Chromatin organization drives the exploration strategy of nuclear factors

Matteo Mazzocca[1]*, Alessia Loffreda[1,2]*, Emanuele Colombo[1], Tom Fillot[1,2], Daniela Gnani[1], Paola Falletta[1], Emanuele Monteleone[1], Serena Capozi[3], Edouard Bertrand[3], Gaelle Legube[4], Zeno Lavagnino[2,5], Carlo Tacchetti[1,2], and Davide Mazza[1,2,6].

Affiliations:

[1] Università Vita-Salute San Raffaele, Via Olgettina 58, 20132, Milan, Italy

[2] IRCCS Ospedale San Raffaele, Experimental Imaging Center, Via Olgettina 58, 20132, Milan, Italy

[3] Institut de Génétique Moléculaire de Montpellier, CNRS, Montpellier 34293, France.

[4] Centre de Biologie Integrative, 118 Route de Narbonne, 31062, Toulouse, France.

[5] Current Address: IFOM ETS– The AIRC Institute of Molecular Oncology – Via Adamello 16, 20139 Milan, Italy

[6] Lead contact. To whom correspondence should be addressed. Email: mazza.davide@hsr.it

Abstract

Nuclear Factors (NFs) rapidly scan the genome for their targets, but the role of nuclear organization in such search is unexplored. To address this, we combined live-cell single-molecule tracking of NFs with multifocal structured illumination of DNA density and characterized the exploration strategy of multiple NFs, including the tumor suppressor p53. p53 alternates between rapid diffusion in the interchromatin compartment (IC) and compact sampling of chromatin dense regions (CDs). This slowed down diffusion – mediated by p53 intrinsically disordered regions (IDRs) – directs p53 to its binding sites in CDs surrounded by IC channels. Efficient targeting requires balanced IDR/chromatin interactions: strong IDRs potentiate target gene activation, but excessive IDR/IDR interactions lead to p53 condensates, derailing its search and downregulating transcription. Our findings highlight the role of NF IDRs on their search and showcase a powerful method to generate traffic maps of the eukaryotic nucleus and dissect how nuclear organization guides NFs action.

Keywords: Single molecule tracking, Chromatin, Nuclear Factors, Search Mechanism.

Running title: Chromatin shapes the NF search.

Introduction

The advances in microscopy approaches and biochemical methods of the last two decades are shedding light on the organization principles of the eukaryotic cell nucleus. DNA/DNA, DNA/RNA and DNA/protein interactions render the nucleus a highly compartmentalized organelle at multiple spatial scales, with different compartments being specialized in peculiar tasks (Amiad-Pavlov et al., 2021; Misteli, 2007; Quinodoz et al., 2021). At the nanoscopic scale, DNA is wrapped into chromatin by nucleosomes, and the chromatin fiber is further organized into a hierarchy of higher-order structures giving rise to topologically associated domains (TADs) and chromatin compartments, that cluster together genes that are similarly regulated (i.e. repressed vs. activated)(Szabo et al., 2019). At a larger, sub-micron scale, the compaction of the chromatin fibers results in chromatin dense domains (CDs) proposed to contain inactive genes, interspersed by a branched network of chromatin-depleted channels, known as the inter-chromatin compartment (IC)(Cremer et al., 2020). Importantly, recent computational and experimental work has highlighted that both active transcription and large macromolecular complexes involved in maintaining the nuclear architecture are preferentially located at the CD/IC interface (Cortini and Filion, 2018; Miron et al., 2020). These observations have led to the hypothesis that the IC might serve as a route for targeting diffusible macromolecules such as transcription factors (TFs) to their site of action (e.g. their binding sites on enhancer/promoters), potentially accelerating their target search mechanism (Cremer et al., 2020).

A rapid search mechanism is particularly relevant for inducible TFs (iTFs) facing the apparently gargantuan task of identifying their target sites among billions of potential decoy sites (Mazzocca et al., 2021a; Woringer and Darzacq, 2018). Remarkably, many iTFs are capable of activating transcription of their target genes in minutes following the activating stimulus (Jana et al., 2021), a timescale that seems incompatible with the classical diffusion-limited search mechanism. Such a target search problem has been addressed extensively in bacteria, where an efficient search is achieved by facilitated diffusion, a mechanism combining 1D sliding on DNA with 3D diffusion (Berg et al., 1981; Esadze and Stivers, 2018; Hammar et al., 2012). Whether TFs exploit a similar 1D+3D search mechanism in the eukaryotic cell nucleus is unclear, as the large excess of nonspecific binding sites, the heterogeneity in chromatin density and the presence of nucleosomes might limit the efficacy of facilitated diffusion.

In recent years, single-molecule tracking (SMT) approaches (Gebhardt et al., 2013; Mazza et al., 2012) have started to shed light on some mechanisms used by nuclear proteins to search for their target sites in eukaryotes (Izeddin et al., 2014; Normanno et al., 2015). In particular, live-cell SMT of proteins involved in the maintenance of chromatin organization (such as CTCF)(Hansen et al., 2020) or its epigenetic state (such as the Polycomb protein Cbx2)(Kent et al., 2020; Tatavosian et al., 2019) display an accelerated search mechanism named guided exploration (Hansen et al., 2020; Mazzocca et al., 2021a). Here, transient

multivalent interactions mediated by the protein intrinsically disordered regions (IDRs) trap the factor in nuclear condensates or clusters that are explored in a compact (exhaustive) fashion.

The role of condensates in transcriptional activation remains however fervently debated (Narlikar et al., 2021). While some data point to condensates as a way to enhance the on-rate of TFs to their binding sites and consequently amplify transcription (Boija et al., 2018; Hnisz et al., 2017), recent findings highlight that condensates could also be detrimental for transcription (Chong et al., 2022). On the other hand, a recent report on artificial TFs suggests that the IDRs per-se, rather than condensates formation, could have a positive role on TF binding and transcriptional activation (Trojanowski et al., 2022).

In this context, whether guided exploration characterizes the dynamics of diverse nuclear proteins/TFs – especially of those not participating in the assembly of visible condensates – and how nuclear organization affects the TF search remain fundamental, yet unaddressed, questions.

To address these questions, we combined SMT of nuclear factors with super-resolved structured illumination (multifocal SIM, mSIM) (York et al., 2012) imaging of a reference channel in an integrated optical microscope allowing for the tracking single molecules within their chromatin environment with 150nm resolution.

We exploited the developed SMT/mSIM microscope to characterize the role of chromatin in shaping the search mechanism of different nuclear proteins, showing that different factors display distinct accessibility to DNA dense regions that strongly correlates with their propensity to interact with immobile scaffolds, such as chromatin itself. We next focused on characterizing the search mechanism of the tumor suppressor p53, a key TF involved in the transcriptional response to DNA damage. Although p53 has been shown to be capable of facilitated diffusion in test tube experiments (Kamagata et al., 2020; Tafvizi et al., 2011), its search mechanism remains unexplored in living nuclei. Our analysis shows that the p53 search is defined by rapid diffusion in the IC and slowed down anisotropic diffusion in CDs, where chromatin-bound p53 molecules are enriched. Notably, the combination of genome-wide analysis of gene expression with chromatin conformation data confirms that chromatin is, on average, slightly more compacted at regulated p53 target genes than at unregulated ones. At the IC/CD boundary, p53 diffusion is slowed down and rendered more anomalous by interactions mediated by p53 IDRs.

To characterize the role of its IDR in p53's target search mechanism we performed SMT on p53 mutants, either without its IDRs, or by fusing the strong IDR from FUS protein to p53. Upon IDR deletion, p53 displays reduced guided exploration, and it is less able to penetrate the regions of higher DNA density, leading to lower expression of its target genes. On the other hand, while the strong IDR can lead to enhanced expression of its target genes, we find that when p53-FUS is expressed at concentrations sufficient to form condensates, the target search is derailed and transcription is repressed. Our results highlight the fact that condensates are not exclusively activating, but can also shut down transcription. We predict that the application of

SMT/mSIM to multiple TFs and chromatin/organelles binding proteins will enable to dissect how the crowded nuclear environment can guide the molecular players involved in transcription, DNA replication and DNA repair to their targets.

Results

Different nuclear factors display different accessibility to DNA dense nuclear regions.

To address how the search mechanism of nuclear factors (NFs) relates to chromatin organization, we designed a microscope capable of combining Highly Inclined Laminated Optical Sheet (HILO) imaging (Tokunaga et al., 2008) of TF dynamics by SMT with super-resolution imaging of a reference channel, by multifocal structured illumination microscopy (mSIM, **Figure S1A**). As detailed in the Methods section, mSIM imaging is based on projecting a pattern of illumination spots on the sample, created by a digital micromirror device (DMD), scanned across a 20x20 μm field of view in 2 seconds. The image is then reconstructed via virtual pinholing (resulting in confocal-like optical sectioning) and pixel reassignment (which increases the lateral resolution of about 1.4x). We confirmed that our gain in lateral resolution is close to the theoretical maximum by imaging microtubules in fixed cells (**Figure S1B**) and that mSIM results in increased optical sectioning by DNA staining using Hoechst 33342 in living osteosarcoma cells (**Figure 1A**). Further, we evaluated that chromatic aberrations between the SMT and the mSIM channels were on average below the resolution limit, when imaging fluorescent beads (**Figure S1C**). Finally, we moved on combining mSIM of DNA density with single molecule imaging of Halo-tagged proteins diffusing in the nucleus of cells (**Movie S1**).

Structured illumination has been recently used to study how different proteins occupy regions of specific DNA density, in fixed samples (Miron et al., 2020). In contrast, our mSIM/SMT microscope allows for the characterization of the dynamical behavior of those proteins in living cells.

To this end, we recorded the positions of the detected Halo-tagged single molecules for each of the tested proteins and measured the Hoechst intensity at each of these positions, classified in quartiles (**Figure 1B-C**). We focused our analysis on one “inert” tracer (unconjugated HaloTag), two TFs (p53 and NF-kB), an architectural protein (CTCF) and a chromatin core component (Histone H2B). The analysis revealed that different factors map against DNA density with different likelihoods. Unconjugated HaloTag was found to be enriched in regions at lower DNA density, while histone H2B was preferentially found at regions with higher DNA density (**Figure 1C**). The TFs and CTCF showed an intermediate profile, with CTCF displaying more enrichment in DNA dense regions than p53 and NF-kB (**Figure 1D**).

The observed differences in protein accessibility to DNA dense nuclear regions did not appear to be caused by size-exclusion effects, as no correlation between protein molecular weight and enrichment in higher DNA classes was observed (**Figure 1E**). Rather, the tendency of NFs to localize in DNA dense region is correlated

to their ability to bind chromatin, as measured by the fraction of bound molecules (Mazzocca et al., 2021b). This suggests that the different localization of the tested NFs might be driven by interactions with scaffolds, such as chromatin itself (**Figure 1F**).

We aimed to identify whether the diffusion speed of each NF is controlled by the DNA density of the visited nuclear regions. To this end, we quantified the instantaneous diffusion coefficient D_{inst} associated to each single molecule displacement and evaluated the probability to observe a certain D_{inst} in each DNA density class (**Figure 1G**).

This analysis revealed two class of nuclear factors with strikingly different dynamic behaviors. H2B and NF-kB are enriched in DNA dense and DNA poor regions respectively, regardless of their diffusion speed. In contrast, for both p53 and CTCF, slow diffusing molecules are enriched in DNA dense regions, while fast diffusing molecules are enriched in DNA poor regions. (**Figure 1G**).

In sum, different NFs can sense DNA density differently, with preferential localization at DNA dense regions being apparently driven by their propensity to interact with nuclear scaffolds, as estimated by the single molecule bound fraction. Further, some factors such as CTCF and p53 are slowed down at regions with higher DNA density, while others preferentially occupy regions at defined DNA density, independently of their diffusion speed.

Different NFs display different search strategies that correlate with their accessibility to DNA dense regions.

Since our results indicated that different nuclear proteins display different mobility in chromatin, we next investigated how these proteins search for their binding sites and whether their search is influenced by chromatin organization. The search mechanism of NFs can be classified under two universal classes: non-compact exploration - where the factor has a high probability of leaving a certain volume before having explored it completely, e.g. in the case of Brownian diffusion - and compact exploration, where the protein exhaustively explores each nuclear region before leaving it, as in the case of diffusion in fractal/crowded environments (Mazzocca et al., 2021a; Woringer and Darzacq, 2018). These different search strategies can be highlighted by analyzing the anisotropy of diffusion - i.e. the likelihood of unbound molecules to walk back on their steps – by calculating the distribution of angles between three consecutive localizations (**Figure 2**). Brownian motion generates isotropic diffusion, while compact exploration would display backward anisotropy.

To compute diffusional anisotropy, we labeled the different nuclear proteins with a photoactivatable ligand (PA-JF_{594}) (Grimm et al., 2016) and acquired photoactivated SMT (paSMT) movies (Manley et al., 2008) composed by 10,000 frames with fast acquisition rate (100 fps), (**Figure 2A** and **Movie S2**) at a low molecule density (1-2 localized molecules per frame). We next tracked the molecules, filtered out immobile/bound

molecules using a Hidden Markov Model approach (variational Bayes single particle tracking, vbSPT) (Persson et al., 2013) and measured diffusional anisotropy using the 'fold anisotropy metric '$f_{180/0}$ (Hansen et al., 2020), describing how many times a molecule is more likely to show backward steps than forward steps (**Figure 2B**).

The tested NFs displayed different degrees of diffusional anisotropy: factors showing poor localization in DNA dense regions display low anisotropy (HaloTag and NF-kB), compatible with non-compact exploration. Differently, factors enriched in DNA dense regions such as CTCF and H2B showed higher diffusional anisotropy, a hallmark of more compact exploration (**Figure 2C**).

Plotting the fold anisotropy metric $f_{180/0}$ as function of the distance run by the molecules highlights that p53, CTCF and H2B display high diffusional anisotropy at a spatial scale of 100-300 nm, and more isotropic diffusion when jumping to longer distances (**Figure 2D**). This behavior, recently named 'guided exploration' (Hansen et al., 2020), occurs when a nuclear protein is trapped transiently in specific areas but is capable of diffusing freely between trapping zones, potentially accelerating its search for target sites. Since our data showed that diffusion of some NFs can be slowed down in DNA dense nuclear areas, we reasoned that chromatin itself could be responsible for transiently trapping these factors. By combining the analysis of diffusional anisotropy with our mSIM imaging of DNA density, we observe that NFs display higher diffusional anisotropy when moving with slow instantaneous diffusion in DNA dense regions (**Figure 2E**). Thus, factors like p53 and CTCF alternate between isotropic and fast diffusion in DNA poor regions with slower and more anomalous diffusion in DNA dense areas.

In summary, factors displaying different enrichment in DNA dense regions display also different search strategies. Proteins with limited accessibility to dense DNA perform non-compact search in the nuclear environment, while the histone H2B - that preferentially occupies DNA dense areas – shows the highest degree of compact exploration. CTCF and p53 perform guided exploration, potentially using DNA as a template: for these factors, slow diffusing molecules are enriched in chromatin dense regions and appear trapped, while fast diffusing molecules are enriched in regions at low DNA density and explore such areas in a non-compact fashion.

p53 searches its target sites by a combination of fast and slow diffusion, and slow diffusing molecules spatially segregate with p53 chromatin bound molecules.

We next focused on characterizing the search mechanism for the tumor suppressor p53, an important TF controlling the cellular response to genotoxic stress. To this end, we genetically engineered the U2OS-derived DIvA cell line (Aymard et al., 2014) to homozygously label the C-terminal of endogenous p53 with HaloTag, by means of CRISPR/Cas9 (Hsu et al., 2014). These cells allow for enzymatic induction of double strand breaks by inducing the translocation of the AsiSI restriction enzyme with Tamoxifen (4-OHT). After verifying that

p53-HaloTag is fully functional (**Figure S2A-D**), we applied single molecule tracking to characterize p53 mobility before and after its activation by DNA damage, induced by ionizing radiation (IR) or AsiSI translocation. In agreement with previous reports (Loffreda et al., 2017; Mazza et al., 2012), the distribution of frame-to-frame displacements for p53-HaloTag (**Figure 3A**) is described by three apparent diffusion coefficients, with medians equal to 0.07, 0.9 and 4.4 $\mu m^2/s$ respectively (**Figure 3B**). The slowest of these three components likely represents DNA binding, since a p53 mutant at the seven residues responsible for specific DNA contacts (p53-mSB) displays a significant reduction in the fraction of molecules involved in such component (see below). Four hours after DNA damage induction by 10 Gy of IR, the fraction of p53-HaloTag molecules bound to chromatin increases, indicating more efficient recruitment to binding sites (**Figure 3B**), and confirming our previous results upon ectopic expression of p53-HaloTag in other cell lines (Loffreda et al., 2017).

The increased recruitment of p53-HaloTag at its binding sites upon IR is associated with a more pronounced 'guided exploration' anisotropy of its unbound population, as we verified following track classification by vbSPT (**Figure 3C**) – after controlling that no misclassification of bound track segments in the diffusing ones was present (**Figure S2E**). Further, the transition probabilities derived from the vbSPT model highlighted that p53-HaloTag molecules reach the bound state ten times more frequently starting from the slow state than from the fast one (**Figure 3D**). Accordingly, bound molecules more frequently co-cluster with slow diffusing ones than with fast diffusing ones, as can be quantified by computing the pair cross-correlation between the localizations assigned to each of the states (**Figure S2F**). While the cross-correlation between bound and fast diffusing molecules closely resembles the one expected from randomly positioned molecules, slowly diffusing molecules spatially segregate at short distance from bound ones (**Figure S2F**). Together, these data indicate that p53 searches for its targets by alternating between fast and slow diffusion modes, with the slow diffusing molecules performing more compact exploration and occupying more frequently nuclear regions that can be bound by the TF.

Bound, slow diffusing and fast diffusing p53 molecules occupy nuclear regions with distinct DNA density.

Next, we combined p53 track classification with the maps of DNA density obtained by mSIM, to highlight how molecules with different mobility preferentially occupy regions at different DNA density (**Figure 4A**). By averaging the normalized distribution of Hoechst signal around each classified p53 single molecule, we could visualize that fast diffusing molecules preferentially occupy DNA depleted regions, surrounded by regions at higher DNA density - such as the channels composing the interchromatin compartment (IC) - while bound molecules are enriched in denser chromatin domains (CDs), surrounded by DNA poor regions (**Figure 4B**) (Cremer et al., 2020). Slow diffusing molecules localize at regions of intermediate DNA density (**Figure 4B**) that might include regions at the IC/CD boundary previously termed as the 'perichromatin' compartment

(Cremer et al., 2020). Activation of p53 by 10Gy IR further promotes the enrichment of p53 bound molecules in DNA dense compartments (**Figure 4B**). Notably, activation of p53 by AsiSI induction of DNA damage recapitulates the previous observations: in these settings p53-HaloTag displays an increased bound fraction (**Figure S3A**), a diffusion anisotropy profile compatible with guided exploration (**Figure S3B**) and positioning of bound p53 molecules at regions of higher DNA density than diffusing ones (**Figure S3C-D**).

Since p53 bound molecules preferentially reside in DNA dense domains, we next verified whether p53 target genes occupy regions of similar density. To this end, we first performed a DNA-FISH experiment on the CDKN1A gene locus, measuring its position relative to chromatin (**Figure 4C**). Interestingly, the CDKN1A locus shows a slight preference for being positioned at dense DNA sites, but close to regions at lower compaction, in agreement with our hypothesis (**Figure 4D**). To generalize this finding, we decided to investigate whether p53 targets are positioned at dense, compact chromatin regions also genome-wide.

To this end, we analyzed a recent Hi-C dataset generated in DIvA cells upon AsiSI-mediated induction of DNA damage (Arnould et al., 2021) by plotting the contact probability of genomic loci with surrounding regions at increasing linear distance (**Figure 4E**). Genomic loci at higher chromatin compaction have higher probability to contact with more distal regions (Cortini and Filion, 2018). We therefore compared the contact frequency of promoters of known p53 target genes (the p53 cistrome, as identified in the meta-analysis in (Nguyen et al., 2018)), to the one measured at both open chromatin regions (identified by extremely occupied targets, xHOTs by multiple TFs (Boyle et al., 2014)) and dense heterochromatin sites (provided by the lamina-associated domain, LADs (Guelen et al., 2008)). Interestingly, promoters of p53 target genes sit in regions at intermediate compaction compared to xHOTs and LADs (**Figure 4F**).

Since p53 typically regulates only a fraction of all its potential targets, we then aimed to identify the subset of p53 genes successfully regulated in our cells. To this end, we generated RNA-seq datasets upon DNA damage by AsiSI in p53 WT and p53 KO DIvA cells, and considered for our analysis genes that were upregulated in the WT sample, since p53 is largely accepted to be a transcriptional activator. We identified 1050 upregulated genes (with fold change ≥ 2 and FDR < 0.05) in our DIvA p53 WT compared to p53 KO cells (**Figure S4A**). Reassuringly, these 1050 genes display an enriched association to the p53 transcriptional network (**Figure S4B**). Intersecting these genes with the p53 cistrome, we identified 124 high-confidence target genes, regulated by p53 in our cells (**Figure S4C**). We next compared the contact frequency of regulated and non-regulated p53 cistrome targets in our cells (**Figure 4G**). Promoters of non-regulated targets occupy lower compaction regions on average, indicating that regulated p53 target sites sit – on average – at regions with higher chromatin density than both non-regulated p53 target genes and regions nonspecifically accessed by multiple TFs.

Thus, p53 scans the nuclear environment by diffusing fast and isotropically in the interchromatin compartment and slowing down, performing more compact exploration of regions at higher DNA compaction, enriched by p53 target sites.

The p53 search mechanism is controlled by interactions mediated by its DNA binding domain and IDR.

To dissect the mechanism controlling the DNA density-guided search strategy of p53, we analyzed the diffusional behavior of HaloTag-p53 mutants, ectopically expressed in a p53 KO DIvA cell line, generated by CRISPR-Cas9 mediated gene editing. Previous reports indicate that the intrinsically disordered regions (IDR) of NFs might be responsible for their target search (Brodsky et al., 2020; Garcia et al., 2021; Hansen et al., 2020). Analysis of the p53 disorder reveals that both the N-terminus and the C-terminus of p53 WT are disordered (**Figure 5A**). We therefore generated HaloTag-p53 mutants lacking either the N terminus (p53ΔN, lacking both its transcriptional activation domain, TAD and the proline-rich domain, PRD) or the C terminus (p53ΔC, lacking the last 30aa of the protein). Notably, p53ΔC has been shown to be incapable of nonspecific sliding *in vitro* (Tafvizi et al., 2011). On the other hand, our initial analysis on different NFs displayed an interesting correlation between the ability of factors to be enriched in DNA dense regions and their bound fraction, which might be a proxy for their affinity to chromatin. We therefore included in our analysis the p53-mSB mutant that is incapable of specific binding on DNA, given that all the seven amino acids responsible for specific contacts with DNA are mutated to alanine (Morisaki et al., 2014). Finally, a mutant lacking both specific binding and its C-terminal region was included (p53-mSB-ΔC). We next collected paSMT movies on these mutants, and analyzed their single molecule dynamics (**Figure S5A**). Mutants involving the DNA binding domain and/or the C-terminal region displayed a significant reduction in the TF bound fraction, associated to an increase in the fraction of diffusing molecules (**Figure S5B**). Further, all tested mutants displayed reduced backward diffusional anisotropy than p53 WT, indicating that both the IDRs and the DNA binding domain of p53 might participate to guiding the TF to its binding sites (**Figure 5B**). Next, we resorted to our SMT/mSIM approach to evaluate the enrichment of these mutants at DNA dense regions of the nucleus. While p53 WT displays an enrichment of bound/slow diffusing molecules in regions at high DNA density, this enrichment is progressively lost, in particular when analyzing the localization of mutants lacking the C-terminal domain of the protein (**Figure 5C**). Thus, in agreement with our previous results on different NFs, interactions (mediated by the p53 IDRs and by its binding domain) control the capability of p53 to reach regions at higher DNA density, where p53 targets are preferentially positioned.

If, indeed, deletion of p53 IDRs disrupts the targeting of the TF to its binding sites, one would expect these mutants to display a lower capability to induce transcription. To test this possibility, we compared the expression of two p53 target genes in cells expressing p53 WT, or p53ΔC (the only mutant displaying

transcriptional activity in luciferase assays (Zhou et al., 1999) over a p53-null background. To account for the cell-to-cell heterogeneity of ectopically expressed p53, we resorted to single-molecule fluorescence in situ hybridization (smFISH), to quantify the number of expressed mRNA molecules at the single cell level and to relate it with the TF protein expression levels (**Figure 5D**). Notably, at similar expression levels of p53, the p53ΔC mutant displayed lower mRNA counts than p53 WT (**Figure 5E**). Such difference across p53 mutants was also reflected at the nascent transcription level, by quantifying the number of transcription sites (TS) per cell, that appear as 1 to 4 bright foci in the nucleus (**Figure 5F-G**). These results are therefore consistent with the hypothesis that the p53ΔC might be less efficiently targeted to its genes, reducing their expression both at the nascent and the mature RNA level.

A strong IDR fused to p53 can modulate and divert the p53 search mechanism.

Since deletion of the p53 IDRs resulted in a reduction of the protein guided exploration signature, we aimed to investigate the effect of adding an exogenous IDR to p53 on the TF search mechanism.

To this purpose, we fused the IDR derived from FUS protein, to the full p53 coding sequence (**Figure 6A**). The generated HaloTag-FUS-p53 construct displayed nuclear localization and, differently from p53 WT, the capability of forming condensates in living cells at expression levels higher than a certain critical concentration (located around the 60-th percentile of our transfected cell population, **Figure 6B-C**). Analysis by Fluorescence Recovery After Photobleaching (FRAP) revealed that these condensates displayed 'solid' properties, since p53 in these clusters displayed a high immobile fraction (**Figure S6**). Notably, even outside of these condensates (where a large fraction of HaloTag-p53 still resides), FUS-p53 displayed slowed-down diffusion compared to p53 WT (**Figure S6**). Accordingly, when analyzing FUS-p53 mobility at the single molecule level by paSMT, this mutant displayed a reduced mobility. The diffusion coefficients of FUS-p53 were reduced (**Figure 6D**), and a larger fraction of FUS-p53 molecules were classified as bound and slowly diffusing (**Figure 6D**), with almost a two-fold drop in the fraction of fast diffusing molecules compared to WT p53. Further, diffusing FUS-p53 also displayed a stronger signature of guided exploration with a more prominent anisotropy peak at spatial scales below 150nm (**Figure 6E**). Taken together, this data indicates that FUS-p53 spends more time in the slow, highly anisotropic, diffusion state, and therefore samples the nuclear environment in a more compact fashion, supporting the notion that TFs IDRs play a major role in determining the search strategy employed by the TF. We next employed the SMT/mSIM combined approach to monitor how this more compact exploration affects the capability of targeting FUS-p53 to DNA dense domains. To our surprise, however, the analysis revealed that - on average - FUS-p53 is not enriched at DNA dense regions, independently on its diffusion coefficient (**Figure 6F**).

We thus applied smFISH to probe the effect of a strong IDR on the transcription of *CDKN1a* and *MDM2*, at the single cell level. p53 WT and FUS-p53 resulted in remarkable differences in the transcriptional output as

function of the TF expression levels. Transcripts of *CDKN1a* and *MDM2* were found to increase with p53 WT levels, as expected for a transcriptional activator (**Figure 6G**). The amount of synthesized mRNA in response to FUS-p53 displayed instead a more peculiar profile: at expression levels lower than a critical concentration *CDKN1a* and *MDM2* mRNA counts increased with FUS-p53 more markedly than with p53 WT (**Figure 6G**). This more rapid increase was also observed for the number of active TS observed per cell, suggesting that in this regime of low FUS-p53 expression levels, the targeting of the activator to its regulated genes is enhanced. At FUS-p53 expression levels higher than a critical concentration, we instead observed a decrease in mRNA counts and active TS per cell (**Figure 6G**). This observation was faithfully reproduced in another cellular model (p53KO MCF7 cells (Loffreda et al., 2017), **Figure S7A**). Notably, no modulation in expression depending on FUS-p53 levels was observed for the p53-unrelated house-keeping gene *GAPDH* (**Figure S7B**). Of note, the FUS-p53 concentration at which transcription starts to be inhibited, was found between the 50% and the 67% percentile of our cell population, roughly matching with the one at which visible FUS-p53 condensates appear (**Figure 6C**). This data suggest that IDR-mediated interactions need to be finely regulated in order to promote the targeting of the TF on its binding sites, as an excess of strong IDR-containing p53 could divert the search mechanism and inhibit transcriptional activation. To test this hypothesis we therefore re-analyzed our SMT/SIM acquisition on FUS-p53 by splitting the dataset in two subgroups: cells expressing FUS-p53 at low levels, with no visible condensation and cells expressing FUS-p53 at high levels and displaying two or more condensates (**Figure 6H**). Such analysis highlighted that bound/slow-diffusing FUS-p53 can be targeted to regions at higher DNA density when expressed at low levels, while high expression of FUS-p53 derails this targeting, resulting in the localization of both diffusing and bound p53 molecules in chromatin poor regions.

In summary, our data demonstrate that DNA density modulates the target search of p53, through interactions with the protein IDRs, and these interactions need to be finely regulated since both IDR deletions or potentiation can have detrimental effects on p53 targeting and on transcription of its target genes.

Discussion

How TFs scan the genome to identify the subset of their responsive elements to bind and regulate, and what is the role of chromatin organization in directing this search in eukaryotes are fundamental unanswered questions. To address these questions, we have developed a microscope that allows the overlay of single molecule tracks of TFs on maps of chromatin organization obtained by structured illumination. We used the microscope to characterize how DNA density modulates the search process of different NFs, with particular attention to the search mechanism of the tumor suppressor p53.

Our data show that individual NFs display distinct accessibility to DNA dense regions. Some factors such as the NF-kB subunit p65 and inert tracers as the unconjugated HaloTag are excluded from chromatin-dense

regions and display isotropic diffusion. Others, such as p53 and CTCF, display a specific enrichment of slow, anisotropically diffusing molecules in DNA dense nuclear regions, suggesting that these factors might be trapped in these DNA areas, to search for their target sites.

Indeed, our further characterization of p53 diffusion at endogenous levels, revealed that the search mechanism of this TF is compatible with a guided exploration mechanism. p53 alternates between a fast, non-compact exploration mode to a slower diffusion where molecules sample ~100nm sized domains exhaustively by frequently walking back on their steps, as evidenced by p53 anisotropic diffusion at short spatial scales. These slow and anisotropically diffusing molecules scan and interrogate the genome to identify their target sites, since they frequently co-localize with bound molecules. Such guided exploration appears to be modulated upon p53 activation by DNA damage and can speed up the search mechanism, as a CTD deletion mutant with reduced anisotropic diffusion displayed reduced efficiency in the activation of target genes.

Guided exploration, is emerging as a common strategy to accelerate the search mechanism of nuclear proteins: for example the chromatin factors CTCF (Hansen et al., 2020) and the Polycomb subunit CBX2 (Kent et al., 2020) display similar anisotropic diffusion profiles to the ones measured here for p53. However, while CTCF forms nuclear clusters (Hansen et al., 2017) and CBX2 form nuclear condensates that act as trapping zones for the guided exploration mechanism, p53 WT does not appear to be involved in the formation of visible clusters.

Rather, our combined SMT/SIM approach points to chromatin itself as the template for p53 guided exploration. p53 fast diffusing molecules are preferentially localized in DNA poor nuclear regions (i.e. the interchromatin compartment) while slow-scanning molecules appear to diffuse on regions at higher DNA density - potentially representing the surface of chromatin dense (CD) regions - and bound molecules often localize inside or at the edge of these CD domains. This result might reflect the behavior of p53 as a pioneer factor that bind responsive elements in inaccessible chromatin dense regions (Lidor Nili et al., 2010; Sammons et al., 2015), with recent reports highlighting that p53 can act as a pioneer factor only at nucleosome dense regions flanked by nucleosome poor ones (Laptenko et al., 2011; Yu and Buck, 2019).

Mutant analysis for p53 further evidenced that the IDRs of the TF play a role in controlling such guided exploration, as p53 versions lacking IDRs display impaired guided exploration and mislocalization of bound molecules with respect to chromatin environment. This provides new evidence on the emerging role of IDRs in driving the mobility of TFs and, in turn, their targeting process. In agreement with our observations on p53, SMT analysis has been recently used to show that the Hypoxia-Inducible Factor (HIF) 1-α and HIF 2-α display interchangeable nuclear mobility when swapping their IDRs (Chen et al., 2022). Importantly, mutants of the yeast TFs Msn2 and Yap lacking the DNA binding domain, can still locate most of their target genes through their IDRs (Brodsky et al., 2020).

In the last years, TF IDRs have drawn substantial attention also related to the capability of disordered proteins to form condensates that might enhance transcription by increasing the local concentration of the TF (Boija et al., 2018). Recent data highlight that IDRs might be important for the transactivation potential of TFs independently on their capability to form condensates (Trojanowski et al., 2022) and overexpression of an isolated IDR that can interact with specific TFs can divert the TFs search (Chong et al., 2022). Our results extend these observations. When fusing p53 to a strong IDR (derived from FUS), we observed that the strong IDR potentiates guided exploration and the transcription of target genes at low expression levels. However, higher expression of FUS-p53 leads to the formation of solid FUS-p53 condensates and results in the derailment of the search process. In these conditions, FUS-p53 bound molecules do not localize any longer in DNA dense regions and we observe downregulation of target gene transcription.

These results point to a model in which IDR-mediated interactions with the eukaryotic nuclear environment need to be finely balanced to warrant efficient targeting. According to this, p53 mutants deficient in IDR-mediated interactions explore the nuclear environment in a less compact fashion and are less likely to find their binding sites, but strong IDR interactions result in excessively compact search that sequesters the TF away from its responsive elements. A similar trade-off has been described for facilitated diffusion, the most studied accelerated search strategy in prokaryotes (Berg et al., 1981; Esadze and Stivers, 2018; Hammar et al., 2012). Here, optimal search is achieved when the factor spends 50% of the search time by sliding on DNA, as shorter or longer sliding times result in inefficient targeting (Mirny et al., 2009).

Such model raises some novel and important questions we hope to be capable to address in the near future.

First, it will be important to identify what mechanism is controlling p53 guided exploration at DNA dense regions. One compelling hypothesis is that this behavior is the macroscopic manifestation of facilitated diffusion as p53 is one of the few eukaryotic TFs that have been shown to be capable of sliding on DNA in-vitro, and such sliding is mediated by the disordered C-terminal domain of the protein (Tafvizi et al., 2011). Unfortunately, the small length scale on which 1D diffusion on DNA is supposed to occur in living cells hampers the direct visualization of the sliding process in living cells. Another interesting candidate that might mediate p53 compact exploration at CD edges is nascent RNA, since IDR/RNA interactions have been speculated to control the guided exploration of other NFs (Hansen et al., 2020), and the CDs edges have been recently shown to be enriched in nascent RNA (Miron et al., 2020). Experiments attempting to characterize the p53 search upon transcriptional inhibition are challenging, since treatment of cells with drugs interfering with transcription have been shown to also perturb chromatin organization at the micron scale (Hilbert et al., 2021). p53 search may be shaped also by protein/protein interactions, as for example histone modifications marking active chromatin, general transcription factors and members of the pre-initiation complex are found to be enriched at the boundary of CDs (Miron et al., 2020).

Second, guided exploration might concur to the target selectivity of p53 allowing p53 to activate transcription of only those target genes in the 'correct' chromatin environment. It is – for example – tempting to speculate that p53 targets could reposition inside or outside of CDs in response to specific stimuli, and such repositioning would determine whether the target will be found and transcribed. It is conceivable that live-cell labeling of endogenous DNA sequences (for example using approaches based on fluorescently tagged enzymatically dead CRISPR/Cas9 (Ma et al., 2018; Qin et al., 2017) could be instrumental to address this compelling hypothesis.

Another important question is whether the search mechanism that we describe here for p53 also applies to other transcription factors. On one side, the CD/IC interface appears as a peculiar compartment, enriched with nascent RNAs and permissive histone marks (Miron et al., 2020), and it appears therefore possible that many other factors would be targeted there with high efficiency. To a limited degree, however, literature data on other nuclear proteins seem to point against a common shared search mechanism. Factors such as the oncogene cMyc (Izeddin et al., 2014) and the NF-kB subunit p65 (this work) apparently displays non-compact search mechanisms, while P-TEFb displays compact-exploration at all spatial scales (Izeddin et al., 2014). Finally, other NFs display 'guided exploration' that depends on the capability of the factor to form clusters (Hansen et al., 2020; Kent et al., 2020). Different TFs are likely to explore the nuclear environment differently, by transiently interacting with different nuclear structures, organelles/compartments and molecular players. We envision that by increasing the throughput of the SMT/mSIM approach described here for probing multiple nuclear organelles, it will be possible to map the specific nuclear landscape sensed by any individual TF.

Methods

Cell culture

DIvA cells (originated from the human osteosarcoma U2OS) were a kind gift from the Gaëlle Legube lab (Aymard et al., 2014). The U2OS-derived line with endogenous expression of CTCF-HaloTag (used by us for control experiments), was a kind gift from the Tjian and Darzacq group (Hansen et al., 2017).

All cell lines, including those that we derived by CRISPR/Cas9 from DIvA, were cultured in DMEM (Thermo-Fisher, cat. 31053044) supplemented with 10% heat-inactivated Qualified Fetal Bovine Serum (Gibco), 100 units/mL penicillin-streptomycin (Thermo-Fisher, cat. 15140122) and 2 mM L-Glutamine (Gibco, Thermo-Fisher, cat. 25030081). For DIvA and DIvA-derived cell lines, DMEM was further supplemented with 1µg/mL puromycin (Thermo-Fisher, cat. A1113803).

Cells were grown at 37°C in a humidified incubator with 5% CO_2. For routine maintenance, cells were passaged every 2-3 days by trypsinization, plated on 75-cm flasks, and tested once a week for mycoplasma contamination (PCR-based assay).

Generation of cell lines

CRISPR/Cas9 gene editing was used to create p53-HaloTag knock-in (KI) and p53 knock-out (KO) cell lines.p53 KI DIvA cells were generated using four plasmids (kind gifts from Edouard Bertrand lab) encoding the Cas9-D10A nickase (Cong et al., 2013), two guide RNAs (sgRNA1 and sgRNA2) and a repair vector carrying both the HaloTag gene and a neomycin resistance gene, flanked by two p53 homology arms (~800 bp). The sequences targeted by sgRNA1 and sgRNA2 on the p53 genomic locus were 5' GATGACATCACATGAGTGAG 3' and 5' CAGCCACCTGAAGTCCAAAA 3', respectively. DIvA cells seeded on a 6-well plate were co-transfected with the four plasmids (625 ng of each vector per well) using Lipofectamine 3000 (Thermo-Fisher, cat. L3000008) and following the manufacturer's protocol. After transfection, cells were left to recover a few days before two rounds of antibiotic selection (mild, 4 days and long, ~15 days) with geneticin (G418 Sulfate, Thermo-Fisher, cat. 10131027, used at 800 µg/mL). Cells were next seeded at single cell per well (96 well plate) to isolate single clones. The KI clone used in this study was functionally tested for nuclear localization and abundance of p53-HaloTag, for the absence of untagged p53 and for the capability to induce canonical p53 target genes (both at the RNA and protein level) (**Figure S2**).

To generate p53 KO DIvA cells, a commercial CRISPR/Cas9-based gene editing kit was employed (Santa Cruz Biotechnology, cat. sc-416469-NIC) including constructs expressing Cas9-D10A nickase, two sgRNAs and a GFP marker transiently expressed for selection. DIvA cells were transfected with UltraCruz Transfection Reagent (sc-395739) following the manufacturer's instructions and sorted for GFP the next day. Single clones were isolated and expanded from the sorted population. Successful knock-out of the p53-null clone employed in this work was confirmed by absence of p53 and inactivation of p53 target genes (both at the RNA and protein level) (**Figure S2**).

Plasmids and Transient Transfections

Plasmids expressing HaloTag-p53 mutants (deletions of the p53 TAD, CTD or both; insertion of the FUS N-terminal domain) were synthesized and sequenced by the Genewiz Company from a pFN22A vector (Promega) containing the insert HaloTag-p53 WT. The vectors expressing other HaloTag-conjugated proteins were: H2B (pFC15A backbone, Promega) (Mazza et al., 2012), the NF-κB subunit p65 (pFN22K, Promega) and HaloTag itself (pHTN, Promega).

Plasmids were transiently transfected in p53-null cells. Briefly, DIvA p53 KO cells were seeded at ~30% of confluence, and 24h later (~60% confluence) were transfected with Lipofectamine 3000 (Thermo-Fisher, cat. L3000008), according to the manufacturer's protocol.

DNA damage to activate p53

To stabilize p53 and induce a p53-mediated transcriptional response, DIvA cells were exposed to DNA damage either by 10 Gy γ -irradiation (using a ^{137}Cs source, Biobeam 2000) or through the nuclease enzyme AsiSI-RE, activated upon treatment with 300nM 4OHT (Sigma-Aldrich, cat. H7904). Live imaging experiments on p53 were performed in a time-window between 4 and 5 hours post irradiation or 4OHT treatment.

Western blotting

Cells cultured on 10-cm dishes were washed one time in cold PBS and lysed in 300 µL RIPA buffer (25 mM Tris HCl pH 7.6, 150 mM NaCl, 1% Sodium deoxycholate, 1% Triton X-100, 2 mM EDTA dihydrate) supplemented with protease inhibitors (Sigma-Aldrich, cat. 4693124001). Samples were next incubated at 4°C for 20 min under constant rotation, centrifuged at 12000 rcf and the supernatants were then collected. Protein lysates were quantified by BCA assay (Thermo-Fisher, cat. 23225), loaded on 8% or 12% SDS-polyacrylamide gels and run at 100 V for ~2-3 hours. Proteins were transferred to nitrocellulose membranes in cold transfer buffer (25 mM Tris, 192 mM glycine, 20% methanol) via run at 100 Volts for 2 h at 4°C. Next, membranes were blocked in 5% non-fat dried milk in TBS-T solution (0.1% Tween20 in TBS: 20 mM Tris base, 137 mM sodium chloride, pH 7.6) for 1h at RT while shaking. Membranes were incubated with primary antibodies, all diluted in 5% non-fat dried milk in TBS-T solution. The antibodies employed in this study were: mouse monoclonal anti-p53 DO-1 (Santa Cruz Biotechnology, cat. sc-126; 1:3000 dilution, incubated 1h at RT), rabbit monoclonal anti-p21 (Abcam, cat. ab109520; 1:1000 dilution, incubated overnight at 4°C), rabbit monoclonal anti-GAPDH (Abcam, cat. ab128915; 1:50000 dilution, incubated 1h at RT), mouse monoclonal anti-vinculin (Thermo-Fisher, cat. MA5-11690; 1:4000 dilution, incubated 1h at RT). After antibody hybridization, membranes were washed three times in TBS-T (5 min each wash at RT, while shaking) and incubated for 1h at RT with peroxidase-conjugated secondary antibodies (anti-mouse IgG, Cell Signaling, cat. 7076; anti-rabbit IgG, Cell Signaling, cat. 7074) diluted 1:5000 in 5% non-fat dried milk in TBS-T solution. The membranes were finally developed using a ECL substrate (Bio Rad, cat. 1705061) and images were acquired with a CCD camera using ChemiDoc MP imaging system.

RNA extraction and RT-qPCR

Cells grown on 6-cm dishes were washed once in cold PBS and lysed in 750 µL of TRIzol reagent (Thermo-Fisher, cat. 15596018) to extract the total RNA. Lysates were purified using silica membrane columns (Machery-Nagel, NucleoSpin RNA Plus). The isolated RNA was quantified and tested for purity by NanoDrop fluorometer (Thermo-Fisher). For each sample, 2µg of RNA was reverse-transcribed to cDNA using the High-Capacity cDNA Reverse Transcription Kit (Thermo-Fisher cat. 4368814), following the manufacturer's protocol. Real-time qPCR analysis was performed to assess the expression of p53 target genes. Each reaction (20 µL final volume) was composed as following: cDNA (5 µL of 1:100 dilution), 150 nM primers, SYBR Green mix (Roche, LightCycler 480 I Master). To normalize the cDNA amount among different conditions, samples were run altogether using the constitutive gene GAPDH as internal standard.

Single Molecule tracking microscopy

Assembly and characterization of the SMT/mSIM microscope

To acquire SMT movies while collecting reference images of the nuclear architecture, we custom-built a microscope capable of both single molecule imaging of NFs and super-resolved multifocal structured illumination microscopy (mSIM) of a reference channel. The scheme of our SMT/mSIM microscope is depicted in **Figure S1A**. Briefly, the microscope is composed by two illumination arms, connected to a commercial microscope Frame (Olympus IX-71, Olympus Life Sciences). The first illumination arm, directs the laser light from both a 200mW 561 nm laser (Cobolt 06-DPL, Hubner Photonics) and a 200mW 647 nm laser (Coherent Obis, Coherent Inc) to perform SMT using HILO illumination. Here, a movable mirror (MM) in a conjugated plane of the back focal aperture of the objective allows achieving the desired light beam inclination in the object plane (roughly 67°). The second line expands the collimated light from a 405nm and a 488 nm lasers (Coherent Obis, Coherent Inc.) to 0.5 cm in size and directs it onto a digital micromirror device (DMD, Vialux v7000) which creates a pattern of diffraction-limited spots on the sample. The physical size of each DMD micromirror is 13.67 μm and, with the lenses used in our microscope (see scheme in **Figure S1A**), this corresponds to a projected image of each pixel on the sample plane of approximately 117nm. The chosen illumination pattern (an equilateral triangular lattice with side equal to 16 DMD pixels) is scanned over the mSIM field of view. 224 different images are necessary to completely scan the entire field of view. The two illumination arms are next combined through a dichroic mirror(DM)(Di03-R488-t3-25x36, Semrock Inc.) that direct the excitation light to the sample through a quad-band dichroic (Di03-R405/488/561/635-t3-25x36, Semrock inc.) and a 60x 1.49NA oil immersion objective (Olympus ApoN 60x 1.49 Oil, Olympus Inc.). The fluorescent light originated from the sample is collected by the same objective, filtered by the quad-band dichroic and a quad-band emission filter (FF01-466/523/600/677-25, Semrock Inc.) and directed to a sCMOS camera (Orca Fusion C14440-20UP, Hamamatsu Photonics) resulting in an image pixel size equal to 108.3 nm. The microscope is equipped with control systems for temperature (37°C), CO_2 (5%) and humidity, to maintain cells under physiological conditions during live-cell experiments.

We verified that upon reconstruction of the mSIM super-resolved image (see below), the lateral resolution of the microscope increased by a factor higher than 1.4x (**Figure S1B**), and that minimal chromatic aberration (below the microscope resolution limit, **Figure S1C**) was present when imaging subdiffraction fluorescent beads with the two different illumination arms of the microscope.

Reconstruction of mSIM images

As described by York et al. (York et al., 2012), in order to reconstruct a super-resolved and optically sectioned image from the 224 individual frames acquired in our mSIM set-up, it is necessary to: (i) identify the position of the illumination spots in the image plane at each acquisition frame; (ii) perform digital pinholing of the individual frames to get rid of out-of-focus blur; (iii) fuse together the images through pixel-reassignment that result in a $\sqrt{2}$ increase in the lateral resolution of the microscope. All these steps are performed with custom-written routines in Matlab.

Identification of the illumination spot position. The position at which illumination spots appear in the image, does not necessarily correspond to the points in which the DMD spots illuminate the sample, but rather they are the convolution product of the illumination pattern projected on the sample for the actual distribution of fluorescent labels in the sample. On average, however, the distance between the recorded spots should reflect the average distance between illumination points. Similar to what was performed in York et al., we use this principle to find the lattice vectors that describe the 2D displacement between any two illumination spots. The position of all illumination points in the acquisition stack can be defined by two set of vectors (that need to be found for each individual acquisition): (i) the lattice vectors that describe the displacement between an illumination spot and the two nearest neighbor ones; (ii) the offset vectors, that specify the absolute position of the illumination spot closer to the top-left corner of the image in each of the images of the raw acquisition.

Identification of the lattice vectors. To identify the lattice vectors, we first localize the positions at which illumination spots appear in the sample by using the ThunderStorm plug-in in ImageJ/FIJI. These coordinates are then used to generate a stack of binary images with ones at the pixels where the illumination spots have been localized and zero elsewhere. The images are then Fourier transformed and the Fourier magnitude images are then averaged together, giving rise to a periodic lattice of peaks, spaced by the inverse of the average spacing between peaks in the real images. Next, we search for peaks in the Fourier dimension, verify that we can find harmonics of the peaks found at lowest spatial frequency, and identify three candidate peaks with the lowest spatial frequency (that shows harmonics). We next verify that the vector sum and differences of the position vector of these identified peaks, also point to a detectable peak. If two vectors satisfy these conditions they are chosen as the lattice vectors in the Fourier space, and are then Fourier transformed to obtain real lattice vectors.

Identification of the offset vectors. Once we have the lattice vectors, we can find the position of any other illumination spot in one of the images of the raw stack by knowing the position of one of them (i.e. by finding the position of the top left illumination spot in each them image, the offset vectors). To this scope we translate the expected pattern of illumination over the x and y positions and maximize the autocorrelation between the expected illumination distribution and the experimental one.

Virtual Pinholing and pixel reassignment. To suppress out of focus blur, we next perform virtual pinholing, around the positions of illumination spots detected above. To this scope, we scale the raw images of a factor 10 in both dimensions, and we apply a gaussian mask of 130nm in standard deviation around the position of each detected illumination spot. Next, for every frame in the stack and for every spot position in the image the raw data from a squared region around the illumination spot are copied to the final image matrix in a squared region centered to the original coordinates multiplied by two. This procedure is analogous to move the information from each pixel to half of its distance from the illumination center, the principle on which Image Scanning Microscopy (ISM) is based (York et al., 2012). Summing the result of this procedure for each illumination spot generates the final super-resolved image that is then scaled down by a factor 10 and deconvolved using the Richardson-Lucy algorithm.

Given that the illumination pattern is uneven – dimmer at the FOV edge than at its center – and to provide a map for local variations in chromatin density, – the resulting images are then normalized, by dividing the mSIM image for a blurred version (with a gaussian filter with a standard deviation of 2.16 μm) of it.

paSMT acquisition

Two days before paSMT experiments, cells were seeded onto 4-well LabTek chambers (Thermo-Fisher, cat. 155382PK) at a ~30% confluence. One hour before imaging, cells expressing HaloTag-conjugated proteins were labeled with two fluorescent ligands, a photoactivatable (PA) JF_{549} (Grimm et al., 2016) for the SMT videos and the readily photoactive JF_{646} (Grimm et al., 2015) used for collecting a reference image of the nucleus by a red light led source (Excelitas Xcite XLED1, Qioptiq). To this end, cells were incubated for 15 min at 37°C with 10 nM PA-JF_{549} ligand diluted in phenol-red free DMEM. Next, 10 nM JF_{646} ligand was added to the medium, incubating the cells for further 15 min at 37°C. After labeling, cells were thoroughly washed in PBS (two rounds of three washes separated by incubation at 37 °C for 15 min in phenol-red free DMEM).

Photo-activation of the PA-JF_{549} dye was achieved through a 405 nm laser (Coherent, continuous-wave current), with the number of photoactivated molecules (2-3 molecules per frame) tuned by the laser power (0.5-2 mW at the microscope entrance). Photoactivated molecules were excited by a 561 nm laser (Cobolt 60-DPL, 20 mW power at the microscope entrance), adopting stroboscopic illumination to reduce the photobleaching rate and to follow individual molecules for prolonged times. The resulting time-lapse movies (10000 frames per video) were acquired at 5 ms/frame of laser exposure (561 nm laser) and 10ms/frame of camera exposure, to obtain 100 frames per second (fps) movies.

paSMT analysis

Tracking. SMT movies from paSMT acquisitions were analyzed using the ImageJ plugin TrackMate that detects individual spots in each frame of a movie and connects them into tracks (Tinevez et al., 2017). The diffraction limited spots corresponding to single TF molecules are identified by applying a LoG (Laplacian of Gaussian) filter to each frame to suppress noise and signal arising from large structures (e.g. cellular autofluorescence, out of focus background). Spot detection was performed by setting 0.8 µm as maximum molecule diameter and a thresholding value of 5. The identified spots are then connected into tracks, using the LAP algorithm (Jaqaman et al., 2008) that requires to specify the maximal frame to frame displacement for the observed molecular specie. The probability of a diffusing molecule to displace more than a certain distance r_{max}in a time Δt can be calculated as:

$$P(r > r_{max}, \Delta t) = e^{\frac{-r_{max}{}^2}{4D\Delta t}}$$

Where D is the diffusion coefficient of the observed molecule. The maximal frame-to-frame displacement in TrackMate was therefore set using the relationship above, so that less than 1% of the tracks would be missed for typical diffusion coefficients of nuclear proteins (smaller than $5\mu\, m^2/s$)(Lu and Lionnet, 2021). This leads to a maximal displacement threshold $r_{max} = 1\mu m$ in a frame-to-frame time $\Delta t = 10ms$.The control experiments on unconjugated HaloTag were instead analyzed with a maximal displacement $r_{max} = 2\mu m$, since its diffusion coefficient has been reported in the range of $15\mu\, m^2/s$ (Lu and Lionnet, 2021).

TrackMate generated tables providing lists with x, y and t positions for each track. The tables were imported in Matlab and the tracks were analyzed using custom-written routines to: (i) generate and model the distribution of single molecule displacements – in order to extract the abundance of each kinetic subpopulation (indicated as bound, slow and fast fractions in the result section), and their respective diffusion coefficients; (ii) classify individual track segments in one of the three subpopulations using an Hidden Markov model approach, vbSPT; (iii) analyze the co-clustering between bound molecules and diffusing molecules; (iv) analyze the diffusional anisotropy of unbound molecules.

Distribution of single molecule displacements. The tracks generated by TrackMate were used to populate a histogram of frame-to-frame displacements, using a bin size Δr equal to 20nm. The histogram was then normalized (to a probability density function, pdf) to give the probability $p(r)\Delta r$ to observe a molecule moving a distance between $r - \frac{\Delta r}{2}$ and $r + \frac{\Delta r}{2}$ in the time Δt. This probability is then fit by a three component diffusion model:

$$p(r)\Delta r = r\Delta r \sum_{i=1}^{3} \frac{f_i}{2D_i\Delta t} exp\left(\frac{-r^2}{4D_i\Delta t}\right) p(\Delta z, D_i)$$

Where f_i is the fraction of molecules with diffusion coefficient D_i, so that $\sum_{i=1}^{3} f_i = 1$.

In this formulation D_i assumes the value of apparent diffusion coefficient given by the sum of the true diffusion coefficient and a term due to the limited localization accuracy σ^2 in single molecule tracking: $D_i = D_{i,true} + \frac{\sigma^2}{\Delta t}$.

The term $p(\Delta z, D_i)$accounts for the probability that a molecule has to remain within the excitation slice, with thickness $2\Delta z$ which can be calculated as (see Supplementary Note):

$$p(\Delta z, D) = \frac{1}{2\Delta z}$$

Fitting of the cumulative distribution of displacements was performed at the single cell level, and the distributions of obtained parameters ($D_{bound}, D_{slow}, D_{fast}, f_{bound}, f_{slow}$) were plotted as violin-plots using the IoSR-Surrey Matlab toolbox , and compared using Kruskal-Wallis non-parametric testing. P-values were Bonferroni adjusted for multiple comparisons on the 5 different parameters ($D_{bound}, D_{slow}, D_{fast}, f_{slow}, f_{fast}$).

Track classification. To classify p53 tracks into 'Bound', 'Slow diffusing' and 'Fast diffusing' segments, we accumulated data on different cells, isolated tracks lasting longer than 8 frames and gave them as input to the vbSPT algorithm (Persson et al., 2013), by imposing a maximum number of states equal to 3. The algorithm provides the diffusion coefficients for each of the states together with the transition rates between these states. We verified that the diffusion coefficients extracted for each isolated component are in agreement with the ones obtained by the analysis of displacements. Further, we verified that no contamination of bound molecules is present in the diffusing components extracted by vbSPT, which is fundamental in order to correctly analyze diffusional anisotropy.

Co-clustering between bound and diffusing molecules. We evaluated the co-clustering between bound and free molecules by first calculating the centroid of each of the track segments classified as bound and then calculating the cross-correlation between these centroids and all the particle positions belonging to 'slow diffusing' and 'fast diffusing' track segments. These histograms were then compared to the distribution of distances between bound molecules and randomly positioned molecules within the cell nucleus.

Analysis of diffusional anisotropy. To analyze diffusional anisotropy, we removed bound track segments using vbSPT, and we calculated the angle between two consecutive displacements. We then calculated the fold anisotropy metric $f_{180/0}$, a measure of the likelihood that a single molecule will in the backward direction, compared to taking a step forward – calculated as the probability of observing a backward jump (with an angle between jumps in the range $[180° - 30°, 180° + 30°]$), divided by the probability of observing a forward jump (with an angle between jumps in the range $[0° - 30°, 0° + 30°]$). Plotting $f_{180/0}$ as function of the distance run by the molecule allows to discriminate between compact, non-compact and guided

exploration (Hansen et al., 2020). Error bars were calculated as standard deviation from 100 subsampling of the data using 50% of the original data.

SMT/mSIM acquisition

Cells were incubated for 30 min at 37°C with 1 nM JF549 ligand (Grimm et al., 2015) diluted in phenol-red free DMEM. After three washes in PBS, cells were incubated for 10 min at 37°C with Hoechst 33342 (Thermo-Fisher, cat. H3570, 2 µg/mL in PBS) diluted in phenol-red free DMEM. Cells were washed three times in PBS and fresh phenol-red free DMEM was added. Two mSIM images were collected before and after each SMT movie, projecting on the sample a series of 224 patterns of diffraction-limited spots (one pattern per frame) through the 405 nm laser (49 ms/frame laser exposure, 50 ms/frame camera exposure, 20 fps). The SMT movies were acquired using stroboscopic illumination by the 561 nm laser (5 ms/frame laser exposure, 10 ms/frame camera exposure, 100 fps), collecting 2000 frames per movie. Comparison of the two mSIM acquisitions for each cell allows to discard those acquisitions affected by cellular motion or stage drift.

SMT/mSIM analysis

Analysis of the combined SMT/mSIM acquisitions were carried out with custom written Matlab Routines. First, TF tracks are generated from the SMT movie using TrackMate as described above. Next, to each recorded displacement we assigned its instantaneous diffusion coefficients D_{inst} - by dividing the squared displacement for $4\Delta t$ - and the DNA density class, i.e. the quartile of Hoechst intensity at the starting position of the displacements. Heat-maps such as those presented in **Figure 1G** are then calculated by computing the frequency with which displacements with a given D_{inst} fall in each of the four DNA density classes.

For HaloTag-p53 we also analyzed the positioning in DNA of p53 molecules belonging to different diffusion states. To this end, single molecule tracks were sent to the vbSPT algorithm to extract track segments belonging to the 'bound', 'slow diffusion' and 'fast diffusion' states. These classified track segments are then overlaid to the mSIM image of DNA density. Next, the average Hoechst intensity in a 1µm×1µm pixel region surrounding each molecule is calculated separately for each of the three diffusion states of the TF.

Single Molecule In-situ hybridization – acquisition and data analysis

Single molecule Fluorescent In Situ Hybridization (smFISH) was performed to measure nascent and mature RNAs of two p53 target genes (*CDKN1a* and *MDM2*) and the housekeeping gene *GAPDH*. To compare the transcription dynamics of WTp53-HaloTag to p53 mutants, RNA expression was coupled with p53 abundancy quantified via labeling HaloTag during the smFISH protocol. To detect single RNAs, we used HuluFISH RNA probes (PixelBiotech GmbH) -labeled with ATTO-647N fluorophore- for *CDKN1a* and *GAPDH* whereas for MDM2 we employed Design Ready Stellaris probes (Biosearch Technologies) labeled with Quasar 670 dye. The list of smFISH oligos is provided in the Supplementary Table 1. DIvA p53 KO cells were grown on glass coverslips in a 6-well plate and transfected with p53-HaloTag constructs as described above. The day after transfection, cells were fixed in 4% PFA (10 min at RT), and washed with 135 mM Glycine in PBS for 10 min a

RT. Next, coverslips were washed twice in PBS and permeabilized with Triton X-100 diluted in PBS at either 0.1% (cells to be hybridized with *MDM2* probes) or 0.3% (*CDKN1A* and *GAPDH*). After two PBS washes, cells were incubated with a fluorescent HaloTag ligand (2.5 µM TMR –Promega cat. G8251- in PBS) for 1h at RT. To remove the unconjugated TMR, cells were washed with abundant PBS.

Probe hybridization

HuluFISH probes (CDKN1a and GAPDH). Cells were washed twice with HuluWash buffer (2xSSC, 2M Urea), 10 min at RT. Next, cells were hybridized by adding onto coverslips 0.5 µL of probes (either *CDKN1a* or *GAPDH*) diluted in 50 µL of HuluHyb solution (2xSSC,2M Urea, 10% dextran sulfate 5x Denhardt's solution). Hybridization was performed in a humidified chamber at 30 degrees overnight. The following day, cells were washed twice in HuluWash buffer (30 min per wash, at 37 °C in the dark) and then incubated with a DNA staining solution (Hoechst 33342, 1 µg/mL in PBS) for 10 min at RT in the dark. Coverslips were mounted on glass slides with Vectashield (Vector Laboratories) and sealed.

Design Ready Stellaris probes (MDM2). Cells were incubated with 1 mL of the washing buffer A, composed as following: 10% saline sodium citrate (SSC), 20% formamide solution (Thermo-Fisher, ca. AM9342), in RNase-free water (Sigma-Aldrich, ca. 95284). Next, cells were hybridized by adding 1 µL of 12 nM *MDM2* probe diluted in 100 µL hybridization buffer (10% dextran sulfate, 10% SSC-20× buffer, 20% formamide in RNase-free water). Hybridization was performed by incubating cells in a humidified chamber at 37°C overnight. Cells were next washed twice in buffer A (30 min per wash, at 37 °C in the dark), once in 10% SCC-20×, and finally incubated with a DNA staining solution (Hoechst 33342, 1 µg/mL in PBS) for 10 min at RT in the dark. Coverslips were mounted on glass slides with Vectashield and sealed.

Images were acquired with our custom-built widefield microscope (see above), using a 60x oil-immersion objective (N.A.=1.49), a sCMOS camera, and a led source for illumination. Z-stacks composed by 34 images were collected with a 0.3 µm step size along the optical axis.

smFISH analysis

smFISH data was analyzed using the Matlab package FISH-quant. Mature RNA molecules are identified as 3D Gaussian spots with maximal intensity above an arbitrary threshold, that was kept constant for each of the target RNAs analyzed. Nascent RNAs at active transcription sites were identified by looking for high intensity nuclear foci setting the detection threshold so that no more than four actively transcribed loci could be found in each nucleus. This analysis allows to count the number of active transcription sites per cell and to count the number of pre-mRNAs present at the transcription site at the moment of fixation.

DNA FISH

Cell fixation, pre-treatment and permeabilization

DIvA cells seeded in a 24-well plate and grown on coverslip glasses, were washed twice in PBS and fixed using 4% PFA for 10 min at RT. Coverslips were next rinsed three times in PBS at RT (3 min for each wash) and

permeabilized using 0.5% Triton X-100 (diluted in PBS) for 10 min at RT. To remove RNAs that may potentially interfere with the procedure, coverslips were treated with 100 µg/mL RNase A (Thermo-Fisher, cat. EN0531) diluted in PBS, for 1h at RT. Coverslips were then incubated for 1h with 20% glycerol (in PBS) at RT, followed by three consecutive rounds of freezing, thawing and soaking: 30 sec keeping coverslips on dry ice, gradual thawing in ambient air, and 2-min incubation of 20% glycerol at RT, respectively. Cells were thus washed three times in PBS (10 min each, at RT), and incubated in 0.1 M HCl for 5 min at RT. After a washing with 2x Saline-Sodium Citrate buffer (SSC, Sigma-Aldrich, cat. S6639), coverslips were incubated overnight at RT in a solution of 50% formamide (pH 7.0; Thermo-Fischer, cat. AM9342) diluted in 2x SSC. The next day cells were washed in PBS for 3 min, and treated for 2 min at RT with pepsin (40 units/mL; Sigma-Aldrich, cat. P6887) diluted in 10 mM HCl, to break down cellular proteins and facilitate the entering of the probes. Pepsin was next inactivated by two washes with 50 mM Mg2Cl2 in PBS. Cells were then treated with 1% PFA diluted in PBS for 1 min, followed by a washing step in PBS (5 min), and two washes (5 min each) in 2x SSC at RT. Finally, cells were incubated with 50% formamide in 2x SSC, for 1h at RT.

Probe preparation and hybridization

We used a DNA probe for the CDKN1A locus (CHR6: 36644236-36655116) obtained from Genomic Empire (cat. CDKN1A-20-OR), and labeled with 5-TAMRA (orange dUTP, 548nm). A probe mix solution was prepared by adding 2 µL of CDKN1A probe and 8 µL of hybridization buffer (Genomic Empire). The mix was denatured at 73 °C for 5 min, followed by 2 min in ice, and next left for 15 min at 37 °C. In parallel, coverslips with cells were warmed at 73 °C for 5 minutes, to denature genomic DNA. After denaturation, 10 µL/sample of the probe mixture was added on a pre-heated slide (73 °C). A coverslip with cells was placed on top of the drop, with cells facing the probe. Coverslips were sealed with rubber cement probes, to avoid the hybridization mix to dry out. Cells were then placed into a humidified chamber, and incubated at 37°C for 16 hours (in the dark) to allow hybridization. The next day, rubber cement was removed from slides and the coverslips were washed with solution A, composed as following indicated: 0.3% Igepal (Sigma, cat. CA-630) diluted in 0.4x SSC. Cells were incubated with solution A at 73°C for 2 min (in the dark), while gently shaking. A second wash was performed with the solution B (0.1% Igepal in 2x SSC) for 2 min (in the dark) at RT, while shaking. Cells were next incubated with a DNA staining solution (Hoechst 33342, 1 µg/mL in PBS) for 10 min at RT in the dark. After three washes in PBS, coverslips were mounted on slides using Vectashield and sealed with nail polish.

Images of DNA FISH were collected using our custom-built microscope (see the previous section), with a 60x oil-immersion objective (N.A.=1.49) and a sCMOS camera. Chromatinized nuclei (stained by Hoechst) were acquired with our high-resolution implementation (mSIM), using a 405 nm laser (49 ms/frame laser exposure, 50 ms/frame camera exposure, 20 fps), collecting 224 images per cell. The description of the mSIM imaging approach is reported in more detail in the next section.

FRAP

Fluorescence recovery after photobleaching experiments were carried out on a Leica SP-8 confocal microscope equipped with a 63x NA 1.4 oil immersion objective, an Argon laser and a white-light laser (WLL). The pixel size was set to 160.1 nm, and timelapses were collected on regions of 256x256 pixels, with a frame time equal to 262 ms. Pre-bleach and post-bleach imaging were collected setting the WLL wavelength at 552 nm, a laser power of 70% and an AOTF value of 7%. The emitted fluorescent signal was collected with a PMT in the spectral bandwidth of 565 nm to 700 nm. Bleaching was performed in a circular region of 2µm in diameter by increasing the WLL AOTF to 100% and by additionally delivering 70% of the 488nm laser line of the Argon laser. 10 prebleach images, 2 bleach iterations and 500 post bleach images were collected. FRAP data was analyzed by using available Matlab routines (Mueller et al., 2008).

RNA-seq

DIvA p53 WT and DIvA p53 KO cells were plated on 6-cm dishes (12 x 10^4 cells/dish, a triplicate per condition, using different vials for each replicate) and grown in DMEM. Two days later, cells were treated with 300nM 4-OHT to induce AsiSI nuclear translocaltion and DNA damage. Five hours after stimulation, cells were collected and the RNA extracted as described above. Sequencing libraries from the extracted mRNA were prepared with the *mRNA Stranded TruSeq* protocol (Illumina) and sequenced via *NovaSeq 6000 SP Reagent Kit* (Illumina, 100 cycles). Sequencing reads were aligned to the reference genome GRCh37 (alias hg19). Differential Gene expression analysis was performed using DESeq2 (Bioconductor)(Love et al., 2014). The identification of differentially expressed genes (DEGs) was performed by calculating fold change (>2) and statistical significance relative to basal or p53 KO conditions, using a false discovery rate below 0.05 (Benjamini–Hochberg procedure).

Analysis of Hi-C data

Contact frequencies were extracted at a 50kb resolution after normalization for coverage (VC) using HiC-Straw(Durand et al., 2016). The compactness index s at each locus of interest (promoters of the p53 cistrome -ST8 in (Nguyen et al., 2018)-, xHOTs (Boyle et al., 2014) and LADs (Guelen et al., 2008), was estimated by plotting the decay in contact frequency as function of the linear distance d from the locus of interest (Cortini and Filion, 2018). Briefly, loci embedded in more compact chromatin have higher chance of interacting with distal chromatin and thus result in a slower decay of the contact frequency.

Author Contributions

Conceptualization: M.M., A.L., D.M. Methodology: M.M. E.C., Z.L., D.M. Software: E.C., E.M., D.M. Validation: M.M., A.L., E.C., S.C. T.F., D.G., P.F. Z.L. Formal Analysis: M.M., E.C., E.M, D.M. Investigation: M.M., A.L. E.C. Resources: M.M., A.L, S.C., E.B., G.L. Writing – Original Draft: D.M. Writing - Review and Editing: M.M., A.L, E.C, T.F., D.G, P.F, E.M, E.B., G.L, Z.L., C.T, D.M. Visualization: M.M., A.L., D.M. Supervision: E.B, C.T., D.M. Project Administration: A.L., Z.L., D.M. Funding Acquisition: D.M.

Acknowledgements

We are grateful to Prof. Anders S. Hansen and Prof. Samuel Zambrano for their insightful comments on the manuscript. The research leading to these results has received funding from AIRC under IG 2018-ID:21897 project – P.I. Mazza Davide and from Worldwide Cancer Research, Grant Reference number 22-0116 – P.I. Mazza Davide. Tom Fillot is funded by a Maria Sklodowska-Curie Innovative Training Network (ITN-PEP-NET, Grant agreement ID: 813282).

Figures

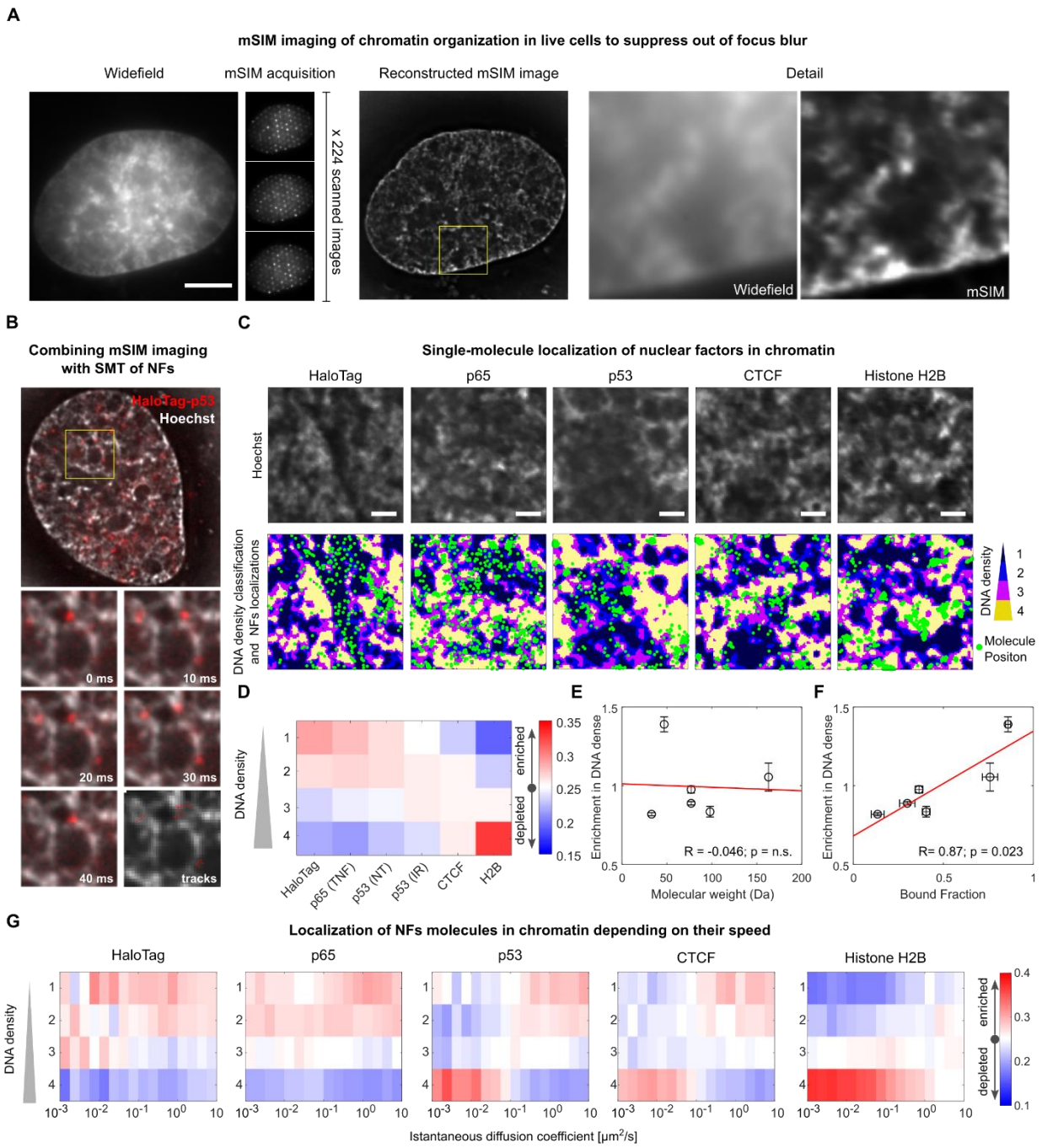

Figure 1. SMT/mSIM experiments to probe the live-cell search mechanism of NFs. (**A**) mSIM imaging is achieved by scanning an array of diffraction limited spots on the sample. Shown is an example of mSIM image of a live cell nucleus labeled with Hoechst 33342, displaying increased optical sectioning compared with Widefield (scale bar 5μm). (**B**) Representative frames of a live-cell acquisition combining mSIM imaging of DNA density with SMT of HaloTag-p53. (**C**) Representative localization of NF molecules on regions with different DNA density. The position of single NF molecules (green dots) is overlaid to the map of Hoechst intensity, classified in quartiles (scale bar 1μm). (**D**) Different nuclear proteins are enriched in regions with different nuclear densities. Enrichment in DNA dense regions does not correlate with the NFs molecular weight (**E**), but does correlate with their bound fraction, i.e. the fraction of immobile molecules (**F**). (**G**) Localization of NFs molecules in chromatin depending on their speed (n_{cells} = 31, 32, 29, 31, 32, for HaloTag, p65, p53, CTCF and Histone H2B respectively, error bars SD).

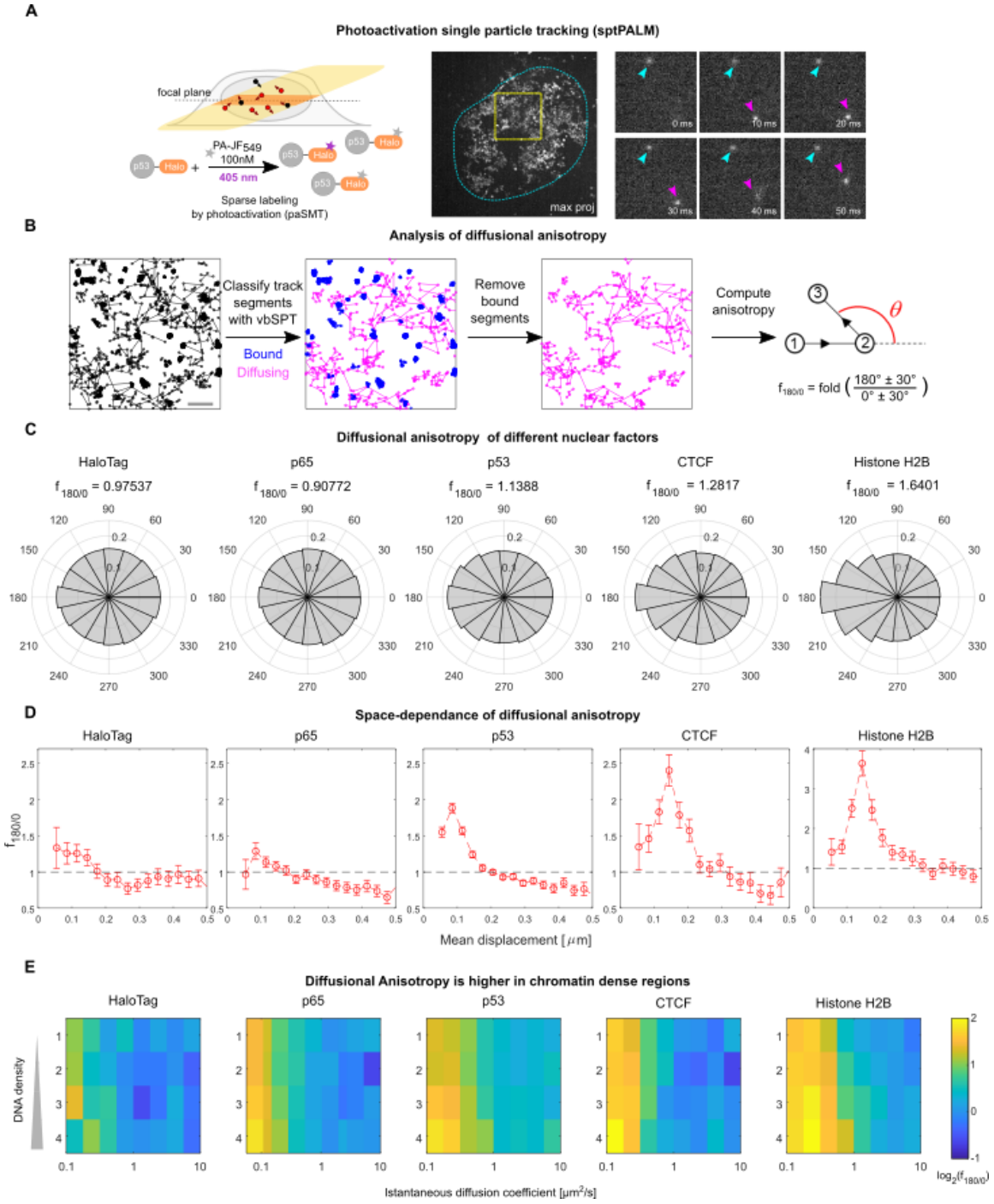

Figure 2. Different NFs display different degrees of anisotropic diffusion. (**A**) paSMT is carried out using highly inclined laminated optical sheet (HILO) microscopy (top left) by labelling the endogenous HaloTag-p53 with the photoactivatable dye PA-JF$_{549}$ (bottom left). Movies, acquired at a framerate of 100fps highlight quasi-immobile chromatin bound molecules (cyan arrowhead) and diffusing ones (purple arrowhead). (**B**) We use vbSPT to classify track segments into bound and diffusing components, and we then focus on diffusing molecules, by computing diffusional anisotropy, by calculating the distributions of angles θ between consecutive jumps, and the fold anisotropy metric, $f_{180/0}$. (**C**) Different NFs display different diffusional anisotropy, with factors poorly localized in DNA dense regions displaying lower anisotropy than factors enriched in DNA dense regions. (**D**) Fold-anisotropy metric $f_{180/0}$ as function of the distance run by the molecules. p53, CTCF and H2B display high diffusional anisotropy at a spatial scale of ~100-150 nm, a signature of transient trapping of these molecules in traps of similar size (n_{cells} = 30, 30, 29, 14, 31, n_{angles} = 59470, 62813, 180414, 26052, 26566 for HaloTag, p565, p53, CTCF and Histone H2B respectively, error bars s.e.m. estimated through boot-strapping). (**E**) Analysis of diffusional anisotropy in our SMT/mSIM data allows to identify that the highest diffusional anisotropy occurs for molecules with slow instantaneous diffusion coefficients in regions at high chromatin density (same data as in **Figure 1 C-G**).

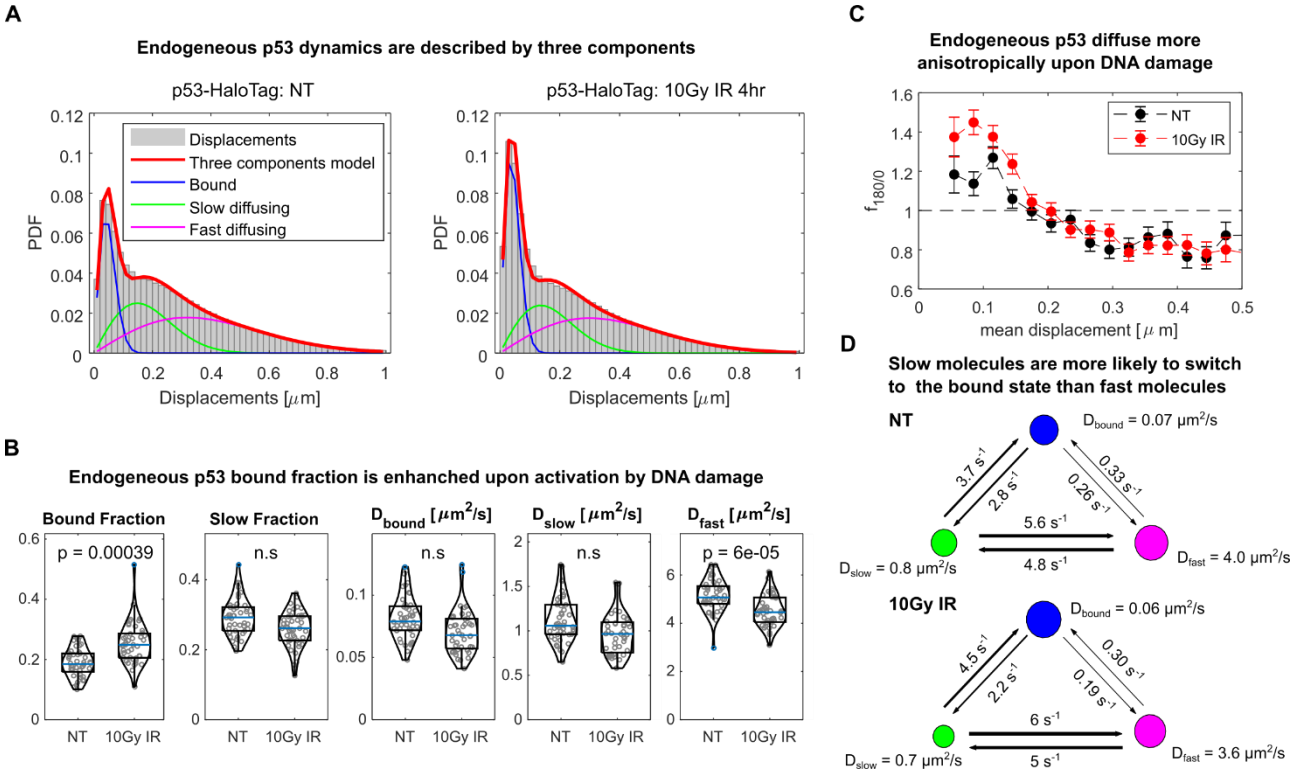

Figure 3. Analysis of single-molecule diffusion of endogenously tagged p53 in DIvA cells. (**A**) The analysis of the distribution of single-molecule displacements before and after the induction of DNA damage via IR shows that p53 is described by three populations, a bound one (blue line) and two diffusing ones (green and magenta lines). (**B**) The parameters extracted by fitting the distribution of displacements show that upon activation of p53 the p53 bound fraction increase, while p53 diffusion is slowed down. (**C**) Upon activation by DNA damage the diffusional anisotropy profile of HaloTag-p53 is compatible with guided exploration. (**D**)The classification of track segments using vbSPT allow to compute the transition probability between the bound state and the two diffusing states. Both before and after activation by IR, p53 molecules are 10x more likely to transition from the slow diffusing state to the bound state than from the fast diffusing state to the bound ones. (n_{cells} = 45, 43 for untreated and 10Gy IR respectively, statistical test Kolmogorov-Smirnov, with Bonferroni correction for multiple testing).

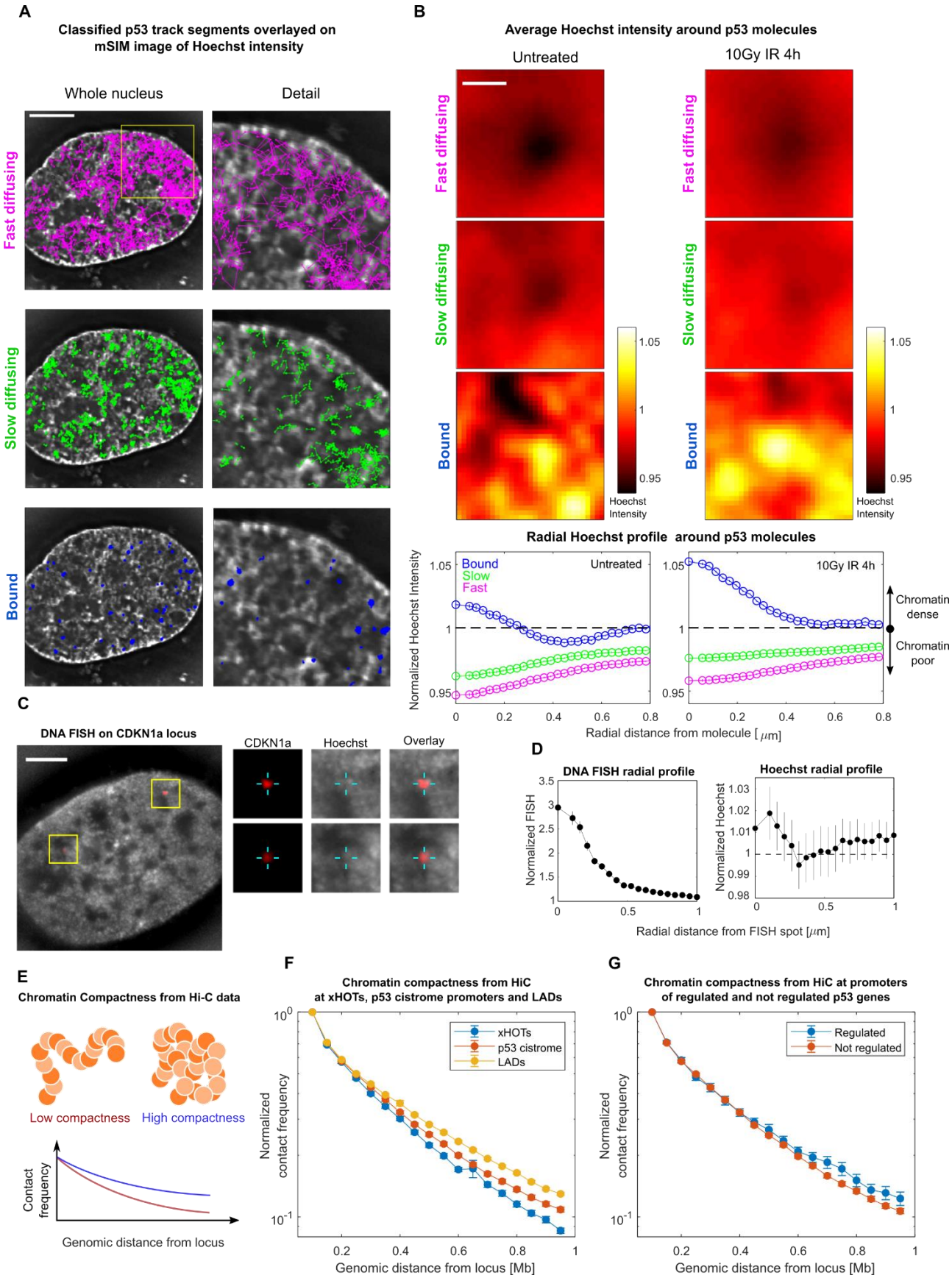

Figure 4 (Legend on next page)

Figure 4. SMT/mSIM experiments highlight that p53 molecules with different diffusivity preferentially occupy regions with different DNA density. (**A**) By overlaying the classified tracks on the chromatin density map obtained by mSIM it is possible to appreciate that bound HaloTag-p53 molecules are positioned within or next to the edges of chromatin dense regions, while fast diffusing molecules are preferentially observed in DNA poor-regions (scale bar: 5µm). (**B**) The same observations can be drawn by plotting the average chromatin radial profile observed around bound, slow diffusing and fast diffusing molecules. Bound molecules sit on chromatin dense regions surrounded by chromatin regions at lower density, while free molecules are enriched in chromatin poor regions surrounded by denser ones, with slow diffusing molecules displaying an intermediate profile between the ones observed for bound and fast diffusing ones. Targeting of p53 bound molecules at DNA dense regions is further enriched upon p53 activation by DNA damage (errorbars, s.e.m. n_{cells} = 29, 29 for untreated and 10Gy IR respectively, scale bar 0.5µm). (**C**) mSIM acquisition of the chromatin surroundings of the *CDKN1A* locus (red: *CDKN1a* locus, grey: Hoechst 33342, scale bar 5 µm Inset show the localization of *CDKN1a* spots). (**D**) We averaged together 2 µm ROIs centered around 31 DNA FISH spots and computed the average radial profile of DNA density. On average, the *CDKN1a* locus appears to be positioned in regions with higher chromatin density than its surroundings (error bars s.e.m). (**E**) Analysis of chromatin compactness at p53 target genes from Hi-C. We analyzed chromatin compaction by plotting the loci contact frequency with surrounding regions as function of the linear distance between them (Cortini and Filion, 2018). (**F**) Promoters of the p53 cistrome are found at regions of intermediate compactness compared to Highly Occupied Targets (xHOTs) and highly inaccessible Lamina associated domains (LADs). (**G**) Further, by stratifying the p53 cistrome into those targets that appear regulated in DIvA cells in our RNA-seq dataset, we observed that p53 regulated target genes are on average in chromatin regions at higher compactness than non-regulated genes (error bars s.e.m).

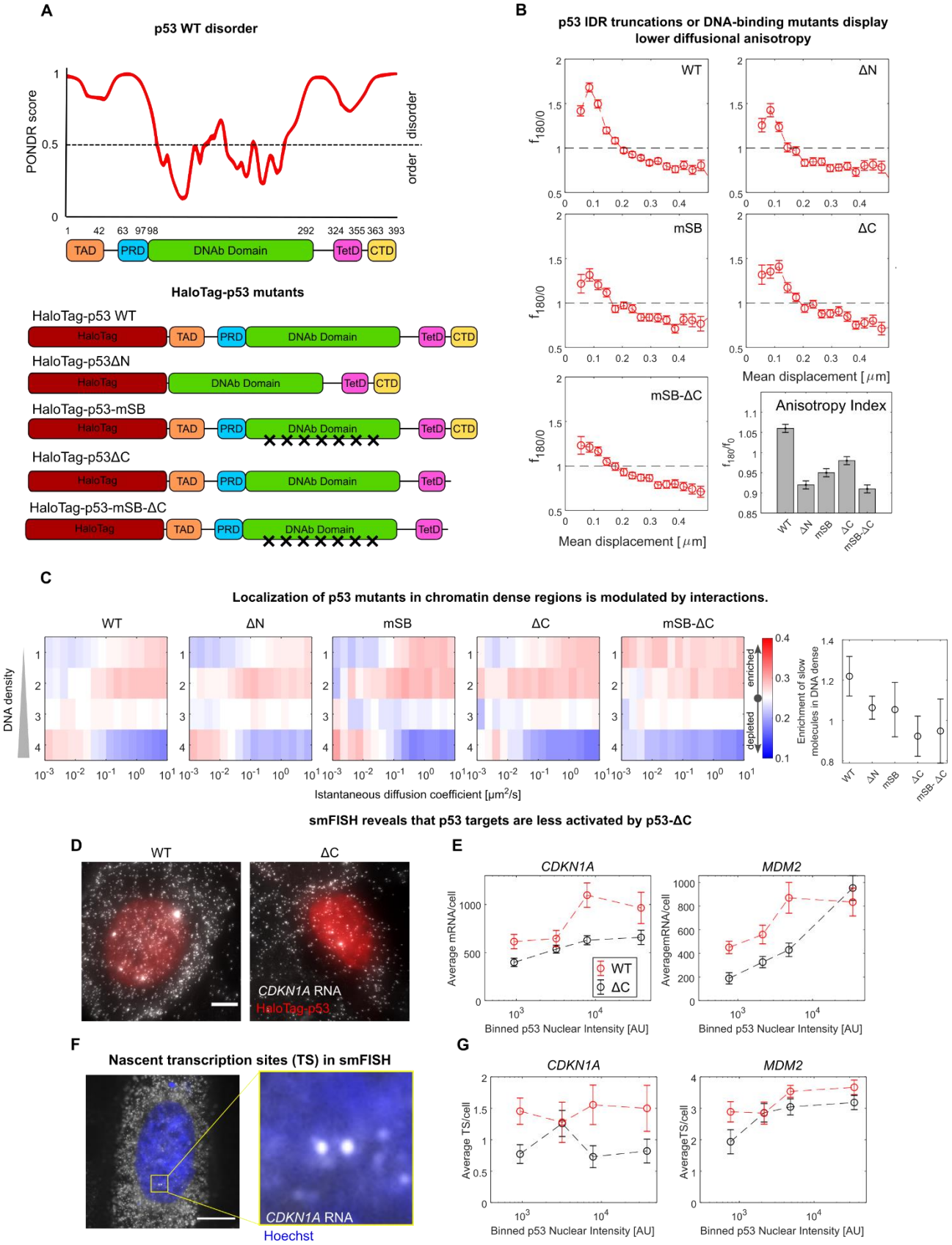

Figure 5 (Legend on next page).

Figure 5. The p53 search mechanism is governed by interactions mediated by its IDRs and DNAb domains. (**A**) Analysis of p53 disorder by PONDR (Top) and list of mutants tested by paSMT and SMT/mSIM. The p53 N-terminal and its C-terminal domain are disordered. (**B**) All tested mutants display reduced diffusional anisotropy compared to WT-p53 (n_{cells}= 45,30,28,24,31, n_{angles}= 262907, 132280,124489, 123006, 153235 for WT, ΔN, mSB, ΔC, mSB-ΔC, respectively). (**C**) SMT/mSIM analysis of the localization of mutant-p53 molecules, shows that the p53 mutants lacking the C-Terminal IDR display impaired recruitment to chromatin dense regions (n_{cells}= 42,34,20,22,9 for for WT, ΔN, mSB, ΔC, mSB-ΔC, respectively). (**D**) smFISH acquisitions to evaluate p53 target gene expression as function of HaloTag-p53 levels. Shown is maximal projection of 3D stack (scale bar 5 μm). (**E**) Evaluation of average mRNA counts for two p53 targets, in cells expressing either HaloTag-p53 WT or HaloTag-p53ΔC, as function of HaloTag-p53 levels (n_{cells}= 74,104,50,88, for WT-*CDKN1a*, ΔC-*CDKN1a*, WT-*MDM2*, ΔC-*MDM2* respectively). (**F**) smFISH allows to count nascent RNA at transcription sites (TS) that appear as bright dots in the nucleus (**G**) Average number of active TS as function of HaloTag-p53 levels s (n_{cells}= 74,104,50,88, for WT-*CDKN1a*, ΔC-*CDKN1a*, WT-*MDM2*, ΔC-*MDM2* respectively).

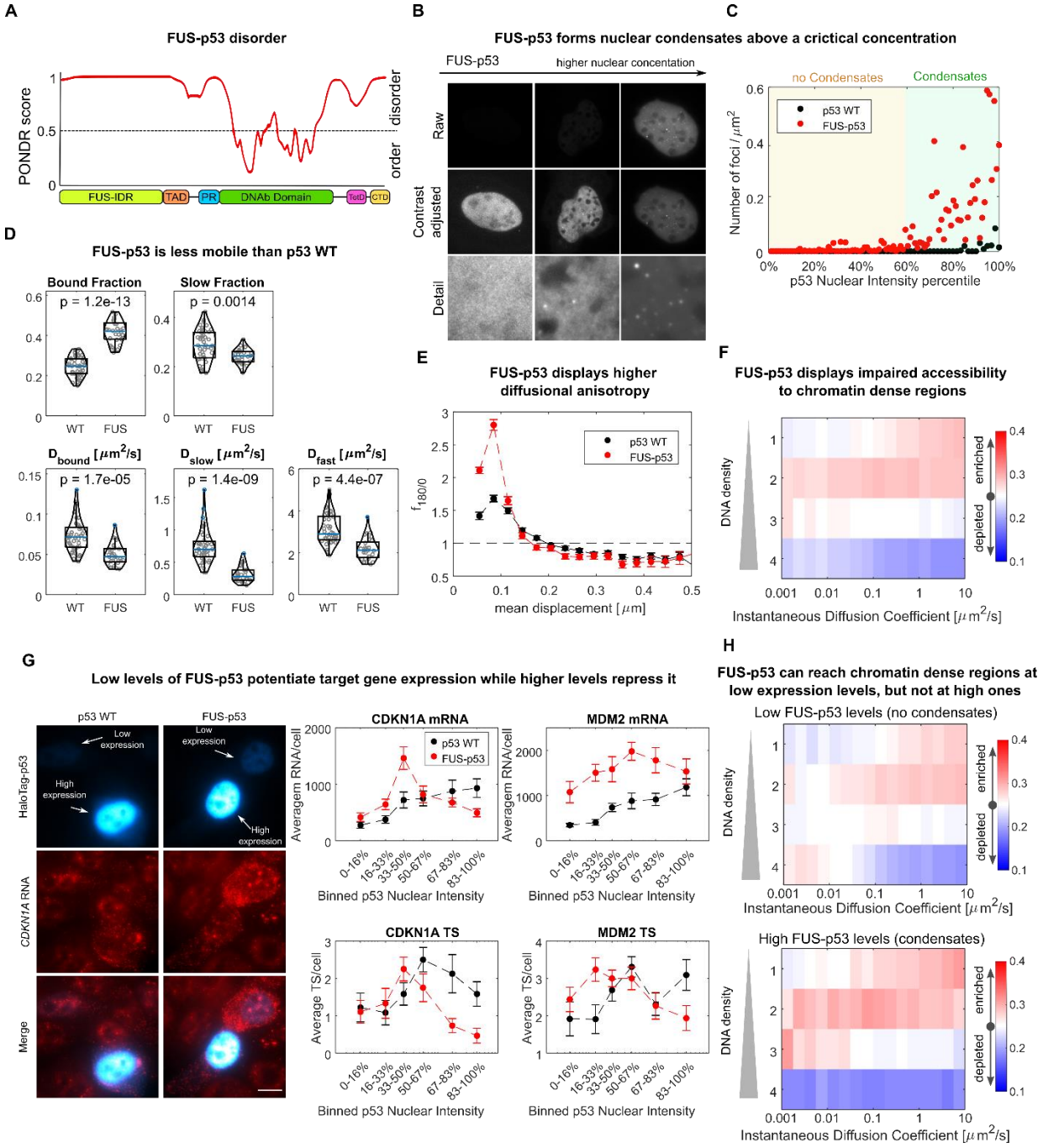

Figure 6. Fusing a strong IDR to p53 renders its diffusion more compact, but interferes with its targeting to DNA dense regions. (**A**) PONDR analysis of the FUS-p53 construct. (**B**) FUS-p53 forms intranuclear condensates above a certain critical concentration that can be estimated (**C**) approximately at the 60th percentile of our transfected cell population. (**D**) paSMT analysis shows that FUS-p53 displays a higher fraction of molecules in bound state, slower diffusion coefficients and (**E**) a more prominent diffusional anisotropy peak (n_{cells} = 45, 29 for p53 WT and FUS-p53 respectively, statistical test Kolmogorov-Smirnov, with Bonferroni correction for multiple testing). (**F**) SMT/mSIM reveals that FUS-p53 accessibility to DNA dense regions is impaired. (**G**) Simultaneous imaging of HaloTag-p53 nuclear levels and mRNA expression by smFISH (False colors are used in the HaloTag-p53 channels to visualize both low expressing and high expressing cells) highlights that p53 target genes are activated in a bimodal fashion by FUS-p53. At low nuclear levels FUS-p53 activates target genes more efficiently than p53-WT, while at higher expression levels FUS-p53 is more repressive. The maximum of target gene expression is found between the 3rd and 4th sextiles of FUS-p53 nuclear levels and roughly matches with the value at which FUS-p53 starts forming visible condensates. (**H**) Stratifying FUS-p53 mSIM/SMT data in cells without and with visible clusters, highlights that FUS-p53 binds regions at higher chromatin density when expressed at low levels, with no visible clusters. (n_{cells} = 22,13 for "no-condensate" and "with condensates" datasets respectively).

References

Amiad-Pavlov, D., Lorber, D., Bajpai, G., Reuveny, A., Roncato, F., Alon, R., Safran, S., and Volk, T. (2021). Live imaging of chromatin distribution reveals novel principles of nuclear architecture and chromatin compartmentalization. Science Advances *7*, eabf6251. https://doi.org/10.1126/sciadv.abf6251.

Arnould, C., Rocher, V., Finoux, A.-L., Clouaire, T., Li, K., Zhou, F., Caron, P., Mangeot, P.E., Ricci, E.P., Mourad, R., et al. (2021). Loop extrusion as a mechanism for formation of DNA damage repair foci. Nature *590*, 660–665. https://doi.org/10.1038/s41586-021-03193-z.

Aymard, F., Bugler, B., Schmidt, C.K., Guillou, E., Caron, P., Briois, S., Iacovoni, J.S., Daburon, V., Miller, K.M., Jackson, S.P., et al. (2014). Transcriptionally active chromatin recruits homologous recombination at DNA double-strand breaks. Nat Struct Mol Biol *21*, 366–374. https://doi.org/10.1038/nsmb.2796.

Berg, O., Winter, R.B., and Hippel, P.V. von (1981). Diffusion-driven mechanisms of protein translocation on nucleic acids. 1. Models and theory. Biochemistry https://doi.org/10.1021/BI00527A028.

Boija, A., Klein, I.A., Sabari, B.R., Dall'Agnese, A., Coffey, E.L., Zamudio, A.V., Li, C.H., Shrinivas, K., Manteiga, J.C., Hannett, N.M., et al. (2018). Transcription Factors Activate Genes through the Phase-Separation Capacity of Their Activation Domains. Cell *175*, 1842-1855.e16. https://doi.org/10.1016/j.cell.2018.10.042.

Boyle, A.P., Araya, C.L., Brdlik, C., Cayting, P., Cheng, C., Cheng, Y., Gardner, K., Hillier, L.W., Janette, J., Jiang, L., et al. (2014). Comparative analysis of regulatory information and circuits across distant species. Nature *512*, 453–456. https://doi.org/10.1038/nature13668.

Brodsky, S., Jana, T., Mittelman, K., Chapal, M., Kumar, D.K., Carmi, M., and Barkai, N. (2020). Intrinsically Disordered Regions Direct Transcription Factor In Vivo Binding Specificity. Molecular Cell *79*, 459-471.e4. https://doi.org/10.1016/j.molcel.2020.05.032.

Chen, Y., Cattoglio, C., Dailey, G., Zhu, Q., Tjian, R., and Darzacq, X. (2022). Mechanisms Governing Target Search and Binding Dynamics of Hypoxia-Inducible Factors. 2021.10.27.466110. https://doi.org/10.1101/2021.10.27.466110.

Chong, S., Graham, T.G.W., Dugast-Darzacq, C., Dailey, G.M., Darzacq, X., and Tjian, R. (2022). Tuning levels of low-complexity domain interactions to modulate endogenous oncogenic transcription. Mol Cell *82*, 2084-2097.e5. https://doi.org/10.1016/j.molcel.2022.04.007.

Cong, L., Ran, F.A., Cox, D., Lin, S., Barretto, R., Habib, N., Hsu, P.D., Wu, X., Jiang, W., Marraffini, L.A., et al. (2013). Multiplex Genome Engineering Using CRISPR/Cas Systems. Science *339*, 819–823. https://doi.org/10.1126/science.1231143.

Cortini, R., and Filion, G.J. (2018). Theoretical principles of transcription factor traffic on folded chromatin. Nature Communications *9*, 1740. https://doi.org/10.1038/s41467-018-04130-x.

Cremer, T., Cremer, M., Hübner, B., Silahtaroglu, A., Hendzel, M., Lanctôt, C., Strickfaden, H., and Cremer, C. (2020). The Interchromatin Compartment Participates in the Structural and Functional Organization of the Cell Nucleus. BioEssays *42*, 1900132. https://doi.org/10.1002/bies.201900132.

Durand, N.C., Robinson, J.T., Shamim, M.S., Machol, I., Mesirov, J.P., Lander, E.S., and Aiden, E.L. (2016). Juicebox Provides a Visualization System for Hi-C Contact Maps with Unlimited Zoom. Cels *3*, 99–101. https://doi.org/10.1016/j.cels.2015.07.012.

Esadze, A., and Stivers, J.T. (2018). Facilitated Diffusion Mechanisms in DNA Base Excision Repair and Transcriptional Activation. Chem Rev *118*, 11298–11323. https://doi.org/10.1021/acs.chemrev.8b00513.

Garcia, D.A., Johnson, T.A., Presman, D.M., Fettweis, G., Wagh, K., Rinaldi, L., Stavreva, D.A., Paakinaho, V., Jensen, R.A.M., Mandrup, S., et al. (2021). An intrinsically disordered region-mediated confinement state contributes to the dynamics and function of transcription factors. Molecular Cell *81*, 1484-1498.e6. https://doi.org/10.1016/j.molcel.2021.01.013.

Gebhardt, J.C.M., Suter, D.M., Roy, R., Zhao, Z.W., Chapman, A.R., Basu, S., Maniatis, T., and Xie, X.S. (2013). Single-molecule imaging of transcription factor binding to DNA in live mammalian cells. Nature Methods *10*, 421–426. https://doi.org/10.1038/nmeth.2411.

Grimm, J.B., English, B.P., Chen, J., Slaughter, J.P., Zhang, Z., Revyakin, A., Patel, R., Macklin, J.J., Normanno, D., Singer, R.H., et al. (2015). A general method to improve fluorophores for live-cell and single-molecule microscopy. Nat Methods *12*, 244–250. https://doi.org/10.1038/nmeth.3256.

Grimm, J.B., English, B.P., Choi, H., Muthusamy, A.K., Mehl, B.P., Dong, P., Brown, T.A., Lippincott-Schwartz, J., Liu, Z., Lionnet, T., et al. (2016). Bright photoactivatable fluorophores for single-molecule imaging. Nat Methods *13*, 985–988. https://doi.org/10.1038/nmeth.4034.

Guelen, L., Pagie, L., Brasset, E., Meuleman, W., Faza, M.B., Talhout, W., Eussen, B.H., de Klein, A., Wessels, L., de Laat, W., et al. (2008). Domain organization of human chromosomes revealed by mapping of nuclear lamina interactions. Nature *453*, 948–951. https://doi.org/10.1038/nature06947.

Hammar, P., Leroy, P., Mahmutovic, A., Marklund, E.G., Berg, O.G., and Elf, J. (2012). The lac Repressor Displays Facilitated Diffusion in Living Cells. Science *336*, 1595–1598. https://doi.org/10.1126/science.1221648.

Hansen, A.S., Pustova, I., Cattoglio, C., Tjian, R., and Darzacq, X. (2017). CTCF and cohesin regulate chromatin loop stability with distinct dynamics. ELife *6*, e25776. https://doi.org/10.7554/eLife.25776.

Hansen, A.S., Amitai, A., Cattoglio, C., Tjian, R., and Darzacq, X. (2020). Guided nuclear exploration increases CTCF target search efficiency. Nat Chem Biol *16*, 257–266. https://doi.org/10.1038/s41589-019-0422-3.

Hilbert, L., Sato, Y., Kuznetsova, K., Bianucci, T., Kimura, H., Jülicher, F., Honigmann, A., Zaburdaev, V., and Vastenhouw, N.L. (2021). Transcription organizes euchromatin via microphase separation. Nat Commun *12*, 1360. https://doi.org/10.1038/s41467-021-21589-3.

Hnisz, D., Shrinivas, K., Young, R.A., Chakraborty, A.K., and Sharp, P.A. (2017). A Phase Separation Model for Transcriptional Control. Cell *169*, 13–23. https://doi.org/10.1016/j.cell.2017.02.007.

Hsu, P.D., Lander, E.S., and Zhang, F. (2014). Development and Applications of CRISPR-Cas9 for Genome Engineering. Cell *157*, 1262–1278. https://doi.org/10.1016/j.cell.2014.05.010.

Izeddin, I., Récamier, V., Bosanac, L., Cissé, I.I., Boudarene, L., Dugast-Darzacq, C., Proux, F., Bénichou, O., Voituriez, R., Bensaude, O., et al. (2014). Single-molecule tracking in live cells reveals distinct target-search strategies of transcription factors in the nucleus. ELife *3*, e02230. https://doi.org/10.7554/eLife.02230.

Jana, T., Brodsky, S., and Barkai, N. (2021). Speed-Specificity Trade-Offs in the Transcription Factors Search for Their Genomic Binding Sites. Trends Genet *37*, 421–432. https://doi.org/10.1016/j.tig.2020.12.001.

Jaqaman, K., Loerke, D., Mettlen, M., Kuwata, H., Grinstein, S., Schmid, S.L., and Danuser, G. (2008). Robust single-particle tracking in live-cell time-lapse sequences. Nat Methods *5*, 695–702. https://doi.org/10.1038/nmeth.1237.

Kamagata, K., Itoh, Y., and Subekti, D.R.G. (2020). How p53 Molecules Solve the Target DNA Search Problem: A Review. International Journal of Molecular Sciences *21*, 1031. https://doi.org/10.3390/ijms21031031.

Kent, S., Brown, K., Yang, C., Alsaihati, N., Tian, C., Wang, H., and Ren, X. (2020). Phase-Separated Transcriptional Condensates Accelerate Target-Search Process Revealed by Live-Cell Single-Molecule Imaging. Cell Reports *33*, 108248. https://doi.org/10.1016/j.celrep.2020.108248.

Laptenko, O., Beckerman, R., Freulich, E., and Prives, C. (2011). p53 binding to nucleosomes within the p21 promoter in vivo leads to nucleosome loss and transcriptional activation. Proceedings of the National Academy of Sciences *108*, 10385–10390. https://doi.org/10.1073/pnas.1105680108.

Lidor Nili, E., Field, Y., Lubling, Y., Widom, J., Oren, M., and Segal, E. (2010). p53 binds preferentially to genomic regions with high DNA-encoded nucleosome occupancy. Genome Res *20*, 1361–1368. https://doi.org/10.1101/gr.103945.109.

Loffreda, A., Jacchetti, E., Antunes, S., Rainone, P., Daniele, T., Morisaki, T., Bianchi, M.E., Tacchetti, C., and Mazza, D. (2017). Live-cell p53 single-molecule binding is modulated by C-terminal acetylation and correlates with transcriptional activity. Nat Commun *8*, 313. https://doi.org/10.1038/s41467-017-00398-7.

Love, M.I., Huber, W., and Anders, S. (2014). Moderated estimation of fold change and dispersion for RNA-seq data with DESeq2. Genome Biology *15*, 550. https://doi.org/10.1186/s13059-014-0550-8.

Lu, F., and Lionnet, T. (2021). Transcription Factor Dynamics. Cold Spring Harb Perspect Biol a040949. https://doi.org/10.1101/cshperspect.a040949.

Ma, H., Tu, L.-C., Naseri, A., Chung, Y.-C., Grunwald, D., Zhang, S., and Pederson, T. (2018). CRISPR-Sirius: RNA scaffolds for signal amplification in genome imaging. Nat Methods *15*, 928–931. https://doi.org/10.1038/s41592-018-0174-0.

Manley, S., Gillette, J.M., Patterson, G.H., Shroff, H., Hess, H.F., Betzig, E., and Lippincott-Schwartz, J. (2008). High-density mapping of single-molecule trajectories with photoactivated localization microscopy. Nat Methods *5*, 155–157. https://doi.org/10.1038/nmeth.1176.

Mazza, D., Abernathy, A., Golob, N., Morisaki, T., and McNally, J.G. (2012). A benchmark for chromatin binding measurements in live cells. Nucleic Acids Res. *40*, e119. https://doi.org/10.1093/nar/gks701.

Mazzocca, M., Fillot, T., Loffreda, A., Gnani, D., and Mazza, D. (2021a). The needle and the haystack: single molecule tracking to probe the transcription factor search in eukaryotes. Biochem Soc Trans *49*, 1121–1132. https://doi.org/10.1042/BST20200709.

Mazzocca, M., Colombo, E., Callegari, A., and Mazza, D. (2021b). Transcription factor binding kinetics and transcriptional bursting: What do we really know? Current Opinion in Structural Biology *71*, 239–248. https://doi.org/10.1016/j.sbi.2021.08.002.

Mirny, L., Slutsky, M., Wunderlich, Z., Tafvizi, A., Leith, J., and Kosmrlj, A. (2009). How a protein searches for its site on DNA: the mechanism of facilitated diffusion. J. Phys. A: Math. Theor. *42*, 434013. https://doi.org/10.1088/1751-8113/42/43/434013.

Miron, E., Oldenkamp, R., Brown, J.M., Pinto, D.M.S., Xu, C.S., Faria, A.R., Shaban, H.A., Rhodes, J.D.P., Innocent, C., de Ornellas, S., et al. (2020). Chromatin arranges in chains of mesoscale domains with nanoscale functional topography independent of cohesin. Science Advances *6*, eaba8811. https://doi.org/10.1126/sciadv.aba8811.

Misteli, T. (2007). Beyond the Sequence: Cellular Organization of Genome Function. Cell *128*, 787–800. https://doi.org/10.1016/j.cell.2007.01.028.

Morisaki, T., Müller, W.G., Golob, N., Mazza, D., and McNally, J.G. (2014). Single-molecule analysis of transcription factor binding at transcription sites in live cells. Nat Commun *5*, 4456. https://doi.org/10.1038/ncomms5456.

Mueller, F., Wach, P., and McNally, J.G. (2008). Evidence for a Common Mode of Transcription Factor Interaction with Chromatin as Revealed by Improved Quantitative Fluorescence Recovery after Photobleaching. Biophysical Journal *94*, 3323–3339. https://doi.org/10.1529/biophysj.107.123182.

Narlikar, G.J., Myong, S., Larson, D., Maeshima, K., Francis, N., Rippe, K., Sabari, B., Strader, L., and Tjian, R. (2021). Is transcriptional regulation just going through a phase? Molecular Cell *81*, 1579–1585. https://doi.org/10.1016/j.molcel.2021.03.046.

Nguyen, T.-A.T., Grimm, S.A., Bushel, P.R., Li, J., Li, Y., Bennett, B.D., Lavender, C.A., Ward, J.M., Fargo, D.C., Anderson, C.W., et al. (2018). Revealing a human p53 universe. Nucleic Acids Research *46*, 8153–8167. https://doi.org/10.1093/nar/gky720.

Normanno, D., Boudarène, L., Dugast-Darzacq, C., Chen, J., Richter, C., Proux, F., Bénichou, O., Voituriez, R., Darzacq, X., and Dahan, M. (2015). Probing the target search of DNA-binding proteins in mammalian cells using TetR as model searcher. Nature Communications *6*, 7357. https://doi.org/10.1038/ncomms8357.

Persson, F., Lindén, M., Unoson, C., and Elf, J. (2013). Extracting intracellular diffusive states and transition rates from single-molecule tracking data. Nat Methods *10*, 265–269. https://doi.org/10.1038/nmeth.2367.

Qin, P., Parlak, M., Kuscu, C., Bandaria, J., Mir, M., Szlachta, K., Singh, R., Darzacq, X., Yildiz, A., and Adli, M. (2017). Live cell imaging of low- and non-repetitive chromosome loci using CRISPR-Cas9. Nat Commun *8*, 14725. https://doi.org/10.1038/ncomms14725.

Quinodoz, S.A., Jachowicz, J.W., Bhat, P., Ollikainen, N., Banerjee, A.K., Goronzy, I.N., Blanco, M.R., Chovanec, P., Chow, A., Markaki, Y., et al. (2021). RNA promotes the formation of spatial compartments in the nucleus. Cell *184*, 5775-5790.e30. https://doi.org/10.1016/j.cell.2021.10.014.

Sammons, M.A., Zhu, J., Drake, A.M., and Berger, S.L. (2015). TP53 engagement with the genome occurs in distinct local chromatin environments via pioneer factor activity. Genome Res. *25*, 179–188. https://doi.org/10.1101/gr.181883.114.

Szabo, Q., Bantignies, F., and Cavalli, G. (2019). Principles of genome folding into topologically associating domains. Sci Adv *5*, eaaw1668. https://doi.org/10.1126/sciadv.aaw1668.

Tafvizi, A., Huang, F., Fersht, A.R., Mirny, L.A., and Oijen, A.M. van (2011). A single-molecule characterization of p53 search on DNA. PNAS *108*, 563–568. https://doi.org/10.1073/pnas.1016020107.

Tatavosian, R., Kent, S., Brown, K., Yao, T., Duc, H.N., Huynh, T.N., Zhen, C.Y., Ma, B., Wang, H., and Ren, X. (2019). Nuclear condensates of the Polycomb protein chromobox 2 (CBX2) assemble through phase separation. J Biol Chem *294*, 1451–1463. https://doi.org/10.1074/jbc.RA118.006620.

Tinevez, J.-Y., Perry, N., Schindelin, J., Hoopes, G.M., Reynolds, G.D., Laplantine, E., Bednarek, S.Y., Shorte, S.L., and Eliceiri, K.W. (2017). TrackMate: An open and extensible platform for single-particle tracking. Methods *115*, 80–90. https://doi.org/10.1016/j.ymeth.2016.09.016.

Tokunaga, M., Imamoto, N., and Sakata-Sogawa, K. (2008). Highly inclined thin illumination enables clear single-molecule imaging in cells. Nat Methods *5*, 159–161. https://doi.org/10.1038/nmeth1171.

Trojanowski, J., Frank, L., Rademacher, A., Mücke, N., Grigaitis, P., and Rippe, K. (2022). Transcription activation is enhanced by multivalent interactions independent of phase separation. Molecular Cell *82*, 1878-1893.e10. https://doi.org/10.1016/j.molcel.2022.04.017.

Woringer, M., and Darzacq, X. (2018). Protein motion in the nucleus: from anomalous diffusion to weak interactions. Biochem Soc Trans *46*, 945–956. https://doi.org/10.1042/BST20170310.

York, A.G., Parekh, S.H., Nogare, D.D., Fischer, R.S., Temprine, K., Mione, M., Chitnis, A.B., Combs, C.A., and Shroff, H. (2012). Resolution doubling in live, multicellular organisms via multifocal structured illumination microscopy. Nat Methods *9*, 749–754. https://doi.org/10.1038/nmeth.2025.

Yu, X., and Buck, M.J. (2019). Defining TP53 pioneering capabilities with competitive nucleosome binding assays. Genome Res. *29*, 107–115. https://doi.org/10.1101/gr.234104.117.

Zhou, X., Wang, X.W., Xu, L., Hagiwara, K., Nagashima, M., Wolkowicz, R., Zurer, I., Rotter, V., and Harris, C.C. (1999). COOH-Terminal Domain of p53 Modulates p53-mediated Transcriptional Transactivation, Cell Growth, and Apoptosis1. Cancer Research *59*, 843–848. .